

Supplementary Information

Critical roles for EGFR and EGFR-HER2 clusters in EGF binding of SW620 human carcinoma cells

Authors

Adam J. M. Wollman^{1,2†}, Charlotte Fournier^{3,4} †, Isabel Llorente-Garcia⁵ †, Oliver Harriman³ †, Alex L. Payne-Dwyer¹, Sviatlana Shashkova^{1,6}, Peng Zhou⁷, Ta-Chun Liu⁸, Djamila Ouaret⁸, Jenny Wilding⁸, Akihiro Kusumi⁷, Walter Bodmer⁸ and Mark C. Leake^{1,9,*}

Affiliations

¹ Department of Physics, University of York, York, United Kingdom.

² Current address: Biosciences Institute, Newcastle University
NE2 4HHO, United Kingdom.

³ Department of Physics, Clarendon Laboratory, University of Oxford, Oxford OX1 3PU, United Kingdom.

⁴ Okinawa Institute of Science and Technology Graduate University (OIST), 1919 Tancha, Onna-son, Okinawa, Japan 904-0495.

⁵ Current address: Department of Physics and Astronomy, University College London, Gower Street, London WC1E 6BT, United Kingdom

⁶ Current address: Department of Physics, University of Gothenburg, 412 96 Gothenburg, Sweden.

⁷ Membrane Cooperativity Unit, OIST, 1919 Tancha, Onna-son, Okinawa, Japan 904-0495.

⁸ MRC Weatherall Institute of Molecular Medicine, University of Oxford, John Radcliffe Hospital, Oxford OX3 9DS, United Kingdom.

⁹ Department of Biology, University of York, York, United Kingdom.

† These authors contributed jointly to this work

* Correspondence should be addressed to M.C.L: mark.leake@york.ac.uk

Supplementary Methods:

Cell lines. From ~100 screened colon carcinoma lines SW620, COLO320HSR and COLO741 all exhibited low endogenous EGFR expression from microarray data (28) (Figure S2) COLO741 was found to be a melanoma and COLO320HSR exhibited transfection instability so SW620 was selected. EGFR protein was undetectable in SW620 by western blotting (Figure S1a), confocal fluorescence microscopy (Figure S1b) and mRNA microarray (Figure S2a). Lysate protein levels were estimated by radio immunoprecipitation and BCA (Thermo Scientific™ Pierce™). Western blotting was performed using anti-EGFR mouse monoclonal (1:1000, clone 1F4, Cell Signaling Technology®) and anti- β -tubulin mouse monoclonal (1:1000, Sigma-Aldrich®) antibodies prepared in TBS-T, 5% milk, incubated overnight at 4°C, then incubated with secondary antibody of polyclonal rabbit anti-mouse conjugated to horseradish peroxidase (Dako) at 1:10,000 and 1:100,000 for EGFR and β -tubulin, respectively, prior to chemiluminescence exposure (Amersham Biosciences). Cell lines with intermediate EGFR expression were used as positive controls.

Plasmid perbB1-EGFP-N1 (donated, Philippe Bastiaens) was used for transformations, comprising human *EGFR* insertion into enhanced GFP backbone pEGFPN1 plus kanamycin resistance. This GFP had no effect on protein clustering compared to the A206K mutant variant in a previous single-molecule study (38). 1 day pre-transfection, 200,000 SW620 cells in 1 ml growth media were seeded into a 12-well plate, adding 2 μ g of pEGFR-EGFP (Invitrogen), 200 μ l Invitrogen Opti-MEM® I Reduced Serum Medium, 1 μ l of Plus™ Reagent and 6 μ l of Lipofectamine® LTX to each. DNA-lipid complexes were added dropwise to cells, incubated 5 h (5% CO₂, 37 °C), then media exchanged to normal the following day. Cells were reseeded onto 15 cm plates in Gibco® Dulbecco's modified eagle media (DMEM) supplemented with 4.5 g/l glucose, pyruvate, L-glutamine and phenol red plus 2 μ g/ml Gibco™ Geneticin® (G418 sulfate). Colonies were isolated using a silicon-cloning cylinder (Corning®), harvested by trypsinization and transferred in a 12-well plate. Flow cytometry-based fluorescence assisted cell sorting (FACS) was used to sort cells into three fractions based on fluorescence intensity using the lowest intensity fraction (i.e., lowest EGFR-GFP expression) for subsequent experiments to minimize effects of expression variability across the cell population. Transgene expression was confirmed by mRNA microarray (Figure S2b), imaging live and immunofluorescently stained fixed cells with confocal microscopy, and western blotting. Confocal fluorescence microscopy confirmed EGFR plasma membrane localization (Figure S1b) and immunofluorescence on fixed cells using AlexaFluor633-labelled anti-EGFR and anti-GFP antibodies further demonstrated colocalization of GFP and EGFR (Figure S3).

EGFR-GFP kinase activity in SW620 cells was confirmed by observing increased phosphorylation of EGFR downstream targets, ERK1/2, in response to EGF (Figure S2b). We used an EGF concentration (either unlabeled or as EGF-RMR in dual-colour TIRF microscopy) equivalent to 100 ng/ml. This level resulted in clear phosphorylation activity on western blots. It is consistent with high physiological levels found in prostate and breast tissue – in particular 50-500 ng/mL found in high EGF bodily fluids including prostate fluid (75) or 30-300 ng/mL found in breast cysts (76).

RT-qPCR indicated low endogenous expression of HER2, HER3 and HER4, and that EGFR-GFP transfection did not cause significant changes in the expression of HER2 and HER3 (Figure S2c).

For CHO-K1, cDNA encoding EGFR tagged with EGFR-Halo was generated by replacing cDNA encoding YFP protein in human EGFR-YFP plasmid (donated, Ivan Nabi), with that of Halo 7-tag protein (Promega), with insertion of a 45-base linker (15 aa, sequence 3SGGG) between EGFR and Halo. cDNA encoding human Erb2 (National Institute of Technology and Evaluation Biological Resource Centre 2-49-10, Nishihara, Shibuya-ku, Tokyo 151-0066 Japan) was fused at its C-terminus with mGFP (EGFP with A206K mutation), placed in the pOSTet153T vector, inserting an 18-base linker (6 aa, with sequence of three SG repeats) between Erb2 and mGFP. All constructs were confirmed by DNA sequencing.

Fab. IgG antibodies to EGF and anti-EGF rabbit anti-mouse polyclonal IgG (Molecular Probes) were digested by papain, confirmed by migration of 28-30 kDa and 25 kDa proteins corresponding to reduced Fc and Fab respectively. Fab was purified using protein A immobilized within a spin column, evaluated by 280 nm absorbance (Thermo Scientific NanoDrop).

Confocal. Zeiss inverted Axio Observer Z1 microscope with LSM 510 META scanning module and Plan-Aprochromat 63x 1.40NA oil immersion DIC M27 objective lens was used, enabling simultaneous imaging of green/red channels via 488 nm/565 nm wavelengths. SW620:EGFR-GFP cells grown in Corning 75 cm² treated plastic cell culture flasks in a humidified incubator (37 °C, 5% CO₂) once 70-100% confluent were sub-cultured by trypsinization. 2-7 days prior to imaging, ~200,000 cells were seeded onto a Ibidi μ -dish 35 mm, high glass bottom using their normal culture media, DMEM, containing phenol red, then changed to DMEM with addition of 4.5 g/l glucose, L-glutamine, HEPES, without phenol red, and supplemented with 10% FBS, 100 units/ml penicillin and 100 μ g/ml streptomycin, or directly into DMEM without phenol red as appropriate. Prior to imaging media was changed to Molecular Probes® Live Cell Imaging Solution supplemented with 1.5 mg/ml G418 sulfate.

For immunofluorescence we harvested SW620-EGFR-GFP cells 48 h prior to fixation at ~50,000 density per well seeded into Ibidi μ -Slide VI0.4, cultured in DMEM without phenol red, supplemented with 4.5 g/l glucose, L-glutamine, HEPES, 10% FBS and 100 units/ml of penicillin and 100 μ g/ml streptomycin, 1.5 mg/ml G418. Cells were fixed with 4% formaldehyde at room temperature for 10min and washed. Non-specific antibody adsorption was blocked with 10% FBS in PBS for 10-20min. Primary antibodies were EGFR (D38B1) XP rabbit monoclonal 4267P (Cell Signaling Technology, 1:50 dilution) and anti-GFP chicken IgY (H+L) (Cell Signaling Technology, 1:400 dilution) in PBS with 10% FBS and 0.1% saponin overnight at 4 °C. Each well was washed with 10% FBS and incubated with secondary antibodies, DyLight 633 goat anti-rabbit immunoglobulin G (IgG) highly cross adsorbed (PN35563, Thermo Scientific), 1:200, and Alexa Fluor 633 goat anti-chicken IgG (H+L) 2 mg/ml (Invitrogen) in PBS with 10% FBS and 0.1% saponin. Channels were washed with PBS and Sigma Aldrich Mowiol 4-88 added to solidify overnight. GFP, DyLight 633 or Alexa Fluor 633 and 4',6-diamidino-2-phenylindole (DAPI) were individually illuminated and scanned (indicating no mycoplasma). GFP was excited as for live cell imaging, while DyLight 633 and Alexa Fluor 633 were excited by a 633 nm HeNe laser.

TIRF. For SW620:EGFR-GFP, a dual-colour single-molecule microscope was modified from previous designs (46) equipped with a nanostage (Mad City Labs) and a 37 °C humidified incubator supplemented with 5% CO₂ (INUB-LPS, Tokai Hit) (Figure S4) We used Elforlight B4-40 473 nm 40 mW and Oxxius SLIM 561 nm 200 mW lasers attenuated into a common path prior to polarization circularization (achromatic $\lambda/4$ plate) before entering a Nikon Eclipse-Ti inverted microscope body. An achromatic lens mounted onto a translation stage controlled the angle of incidence into the objective lens to generate TIRF via a Semrock 488/561nm BrightLine® dual-edge laser-flat dichroic beam splitter into a Nikon TIRF 100x NA1.49 oil immersion objective lens enabling simultaneous GFP/TMR detection across a 20 μ m full width at half maximum field, intensity 1kW/cm², 100nm penetration depth. Fluorescence was sampled 30ms per frame imaging onto two 512x512 pixel array EMCCD cameras (Andor, iXon+ DU-897 and iXon DU-887 for green/red, piezoelectrically cooled to -70°C), 50nm/pixel magnification, via Semrock 561nm StopLine® single notch and Chroma 473 nm notch filters. Typically, scans were 200 frames.

For *in vitro* TIRF we used surface-immobilized GFP or EGF-TMR via anti-GFP or anti-EGF antibodies (Molecular Probes) or Fab followed by BSA passivation prior to washing (34). Slides were constructed from Ibidi sticky-Slides VI0.4 and 25 mm×75 mm No. 1.5 D263M Schott plasma-cleaned glass coverslip and IgG/Fab applied to a single channel and incubated at room temperature for 5min, washed x3 PBS, blocked with 1mg/ml of BSA for 60 min. The channel was again washed x3 then incubated with GFP for 7.5 min or EGF-TMR for 4 min. The channel was

washed x5 before adding 1:10000, 200 nm diameter, 4% w/v, Invitrogen Molecular Probes carboxyl latex beads for focusing.

For live cell TIRF, cells were seeded/grown in media onto glass-bottomed Petri dishes or Corning culture flasks at 37 °C, 5% CO₂. SW620:EGFR-GFP, or SW620 as negative control, imaged on either i) plasma cleaned glass coverslips (25 mm×75 mm No. 1.5 D263M Schott) covered by a sterile Ibidi sticky-Slide VI0.4, or ii) Ibidi μ -dish 35 mm, high glass bottom as for confocal. 48 h prior to imaging, cells were seeded onto the imaging chamber at ~200,000/cm² density. For slides, 50 μ l (or 800 μ l for dishes) DMEM without phenol red supplemented with 10% FBS, 100 units/ml penicillin and 100 μ g/ml streptomycin was added. 24h prior to imaging media was changed to DMEM without phenol red supplemented with 100 units/ml penicillin, 100 μ g/ml streptomycin and 1.5mg/ml G418 sulfate plus inhibitors (2ng/ml cetuximab (BioVision), 10ng/ml trastuzumab (BioVision) or 20ng/ml pertuzumab (Selleck Chemicals)) where necessary, without FBS (starving cells of residual serum EGF) for 24 h. We checked SW620 for expression of the most common ligands, using publicly available RNA-Seq data and our microarray data: EGF zero; TGFA low level; HBEGF low level expression; AREG zero; BTC zero; EREG zero; EPGN no data available (Supplementary). Although we cannot rule out the presence of very low levels of TGFA, cells were washed prior to imaging and no change was observed in EGFR clustering over 60 min unless EGF was added (Figure 3) suggesting no or negligible autocrine EGFR stimulation. Immediately before imaging, media was exchanged to Molecular Probes® Live Cell Imaging Solution supplemented with G418 sulfate and inhibitors where appropriate. Fluorescence sequences at 5min intervals up to 60 min were acquired after adding 100 ng/ml (15.6 nM) EGF-TMR (Molecular Probes). This EGF concentration resulted in clear phosphorylation activity on western blots and is consistent with high physiological levels found in prostate and breast tissue (Figure S2b).

CHO-K1 cells were illuminated using a different TIRF microscope with similar capability. Objective lens-based excitation was used with an evanescent field of 100 nm, and 37°C stage temperature control, around an IX-83, Olympus inverted microscope with Olympus 100× NA1.49 oil immersion objective lens, laser powers 1.2 mW and 5 mW for 488 nm and 642 nm lasers. Dual-colour images were separated by dichroic mirrors (ZT405/488/561/640rpc-UF3, ZT561rpc-UF3 and ZT640rpc-UF3; Chroma), projected into green/red detection channels with emission filters of 500–550 nm for HER2-mGFP (ET525/50m; Chroma) and 662.5–737.5 nm (ET525/50m; Chroma) for EGFR labelled with HaloTag STELLA Fluor 650 ligand (a red fluorescent dye), then onto a two-stage microchannel plate intensifier (C9016-02MERLP24; Hamamatsu Photonics), lens-coupled to a high-speed scientific complementary metal oxide semiconductor sensor camera (C1440-22CU; Hamamatsu), 33 ms per frame. For fluorescence labelling of Halo7-tagged proteins, cells were incubated with 30nM STELLA 650-conjugated HaloTag ligand (GORYO) in Ham's F12 media (Invitrogen), 37°C 20 min, washed x3, and media replaced by Ham's F12 media with 2 mM PIPES, pH7.0.

Tracking. For SW620:EGFR-GFP MATLAB (MathWorks) code (46) was used to track foci in green/red channels to determine spatial localization and calculate integrated pixel intensities and diffusion coefficients. The centroid of each focus was determined using iterative Gaussian masking to sub-pixel precision of 40nm, brightness calculated as the summed intensity inside a 5-pixel-radius centroid-centered circle, after subtraction of local background, signal-to-noise ratio (SNR) defined as intensity divided by background standard deviation. For SNR >0.3 (optimum for high true and low false positive detection from simulations trained on *in vitro* data) a focus was accepted and fitted with a two-dimensional (2D) radial Gaussian to determine its sigma width. Foci detected in consecutive images separated by ≤ 5 pixels and not different in brightness or width by more than a factor of two were linked into the same track. For CHO-K1 foci tracking used a similar algorithm.

Stoichiometry. Stoichiometry per track was estimated in MATLAB using step-wise fluorophore photobleaching to determine GFP or TMR brightness (34) from live cells and corroborated *in vitro*. Live cell foci brightness followed exponential photobleaching. As each focus photobleaches

it will emit the characteristic single GFP or TMR brightness value, I_{GFP} or I_{TMR} , detected as the peak of foci intensities over time. Estimates for I_{GFP} and I_{TMR} were verified by Fourier spectral analysis (34) yielding the same value within error. Initial intensity I_0 was estimated by interpolation of the first 3 points in each track, stoichiometries by dividing I_0 by the single-molecule fluorophore brightness, distributions rendered as kernel density estimations(45). Previous live-cell measurements using the same fluorescent protein (GFP) using photobleaching of all GFP followed by suppression of further GFP expression and then subsequent measurement of any reappearance of fluorescence intensity over a timescale up to 60 min have indicated that the typical proportion of immature GFP is <15% of the total (38), so no correction to stoichiometry was made.

Total Copy Number. The number of EGFR-GFP for SW620:EGFR-GFP on the cell surface was estimated by integration (36) of pixel intensities of the cell area in TIRF corrected for auto-fluorescence using parental SW620 strain. SW620:EGFR-GFP mean pixel fluorescence was calculated for every cell from a region segmented from brightfield using Sobel edge detection, morphologically dilating by a 7-pixel-radius disk to minimize cell-edge effects. Copy number was estimated by multiplying this value over the area of the cell, approximated as a 14 μm -diameter sphere.

Mobility. 2D mean square displacements (MSDs) of tracked clusters were calculated in MATLAB using the centroid positions at time t , $(x(t), y(t))$, considering N consecutive image frames with time interval $\tau = n\Delta t$, where n is a positive integer and Δt is the frame integration time (77):

$$MSD(\tau) = MSD(n\Delta t) = \frac{1}{N-1-n} \sum_{i=1}^{N-1-n} \{ [x(i\Delta t + n\Delta t) - x(i\Delta t)]^2 + [y(i\Delta t + n\Delta t) - y(i\Delta t)]^2 \}$$

$$= 4D\tau + 4\sigma^2$$

The localization precision is $\sigma = (40 \pm 20)$ nm. The apparent diffusion coefficient, D , was estimated from linear fits to the first three points in MSD vs. τ , constrained to pass through $4\sigma^2$ at $\tau = 0$ and allowing σ to vary in the range 20-60 nm.

Colocalization. For SW620:EGFR-GFP cells, colocalization between EGFR-GFP and EGF-TMR was calculated as the overlap integral between green/red foci in MATLAB, whose centroids were within 5 pixels (46). Assuming two 2D normalized Gaussian intensity distributions $g_1(x, y)$ and $g_2(x, y)$, centered around (x_1, y_1) with width σ_1 and centered around (x_2, y_2) with width σ_2 for green and red foci, respectively, the overlap integral v is (46):

$$v = \exp\left(\frac{-\Delta r^2}{2(\sigma_1^2 + \sigma_2^2)}\right),$$

where:

$$\Delta r^2 = (x_1 - x_2)^2 + (y_1 - y_2)^2.$$

Our simulations indicated that green/red foci pairs with identical centroids have an overlap of ~ 0.75 , therefore we used a 0.75 threshold for colocalization detection.

For dwell time analysis in CHO-K1 we used a similar method (78, 79), detecting colocalized green/red foci pairs then measuring the duration over which this separation remained ≤ 180 nm, and generated a histogram distribution of these (denoted “0° image rotation dwell time distribution”) that could be fitted by the sum of two exponential decay functions with time constants $t_1 = 53 \pm 2$ ms and $t_2 = 335 \pm 100$ ms. To determine the time constant associated with random colocalization we rotated the red images by 180° prior to performing the same analysis, indicating a dwell time distribution (denoted “180° image rotation dwell time distribution”) fitted with a single exponential function $t_{\text{rot}} = 52 \pm 2$ ms, identical within error to t_1 , suggesting that t_2 is associated with non-random colocalization. We tested the difference between the “0° image rotation dwell time distribution” and the “180° image rotation dwell time distribution” using a Brunner-Munzel test that indicated very significant differences ($p = 3.1 \times 10^{-5}$).

Modeling foci overlap probability. To assess whether the observed large EGFR clusters could be due to chance colocalization of small clusters combined with our optical resolution limit, we simulated cluster stoichiometry, using experimental fluorescent foci surface densities. Foci were simulated as 2D Gaussians with the same characteristic intensity as *in vivo*, and we used the same noise conditions as measured from real cell images. The probability that ≥ 2 fluorescent foci are separated by less than the optical resolution was determined in MATLAB using a previous model (46). In this model, given a surface density of spots ρ , the probability for a nearest neighbor spot to be within a distance w is given by:

$$p(w) = 1 - \exp(-\pi w^2 \rho),$$

where, for overlapping foci, w is the optical resolution. The resulting probability of overlap can be used to generate the distribution of number of overlaps as a Poisson distribution. The apparent stoichiometry distribution from overlapping foci was then modeled by convolving this Poisson distribution with the expected intensity distribution of an isolated multimer, given by the intensity distribution of a single GFP (Figure S5) width scaled as the square root of the multimer stoichiometry. The latter was obtained by scaling the width of the single fluorophore intensity distribution (Figure S7) by $S^{1/2}$, where S is the model stoichiometry. A random Monte Carlo stoichiometry was generated from several simulated underlying EGFR molecular stoichiometries including monomers, dimers and the mixed oligomer model from Needham *et al.* (47) (51.3% monomer, 21.3% dimer, 10.3% trimer, 5.3% tetramer and 4.1% pentamer). Finally, a population distribution of oligomeric EGFR with stoichiometry sampled from a Poisson distribution with means varying from 1-10 but with broad distributions up to tens of molecules.

Statistics. Two-tailed Student's *t*-tests were performed for comparisons between pairs of datasets to test null hypothesis that data in each was sampled from the same statistical distribution assuming (n_1+n_2-2) degrees of freedom where n_1 and n_2 are the number of data points in each distribution and by convention that *t* statistic values which have a probability of confidence $p < 0.05$ are statistically not significant. For TIRF each cell was defined as a biological replicate sampled from the cell population with sample sizes of 10-117 cells per condition. Technical replicates are not possible with irreversible photobleaching, nevertheless. Pairwise differences between stoichiometry distributions, and of colocalization dwell times, were also assessed using the non-parametric Brunner-Munzel rank order test, for which we assumed that $p < 0.05$ indicates statistical significance. Explicit *p* values are reported where $p > 0.0001$ and not reported below this threshold as they are no longer physically meaningful.

RT-qPCR. To extract RNA, cell pellets were lysed in Trizol (Invitrogen). RNA was converted into cDNA using MMLV reverse transcriptase (New England Biolabs®) with Oligo(dT)12-18 primers (Invitrogen), 10mM dNTP mix and RNase inhibitor Ribolock (Thermo Fisher Scientific), cDNA purified using QIAquick PCR purification (QIAGEN). Expression levels of *HER2*, *HER3*, *HER4* and *EGFR* were determined by qPCR using Fast SYBR Green Master Mix on QuantStudio TM 3 Real-Time PCR System (Thermo Fisher Scientific), 20s/95°C then 40 cycles of 1s/95°C and 20s/60°C, normalized against housekeeping *PLQC2*. Relative fold expression change was calculated using $\Delta\Delta C_t$ analysis.

Microarray.

Microarray expression data were generated by a service provided by the Patterson Laboratory in Manchester, UK. The gene expression data for 78 unique, non-duplicate (not sourced from same patients) colon cancer cell lines were obtained by performing microarray using the Affymetrix GeneChip HG-U133 Plus 2.0 microarray. Data is normalized using RMA and batch-removed using Partek Genomics Suite software. These were compared against publicly available RNA-Seq data (80). For microarray, we developed an algorithmic pipeline with the goal of identifying subpopulations within a given data through a statistical machine-learning method. With this pipeline we statistically determined the expressing and non-expressing subpopulations in our 78 CRC microarray cell line data. The statistically determined background threshold closely matches with the background expression range of 100-150 microarray counts shown in previous work

done by our lab; this therefore defines our background threshold. Expression level below the background threshold was considered as non-expressing.

The results obtained from different probesets for the microarray where available, and for RNAseq, are given below for both the SW620 cell line. In the case of the TGFA ligand we also compared the SW620 output with that of SW480 (a duplicate cell line of SW620 derived from the same patient):

TGFA ligand:

| | SW620 | SW480 | Category |
|--------------------------------|-------|-------|------------|
| Microrarray 211258_s_at | 100 | 81 | Background |
| Microrarray 205015_s_at | 218 | 195 | Very Low |
| Microrarray 205016_at | 360 | 327 | High |
| CCLE RNA-Seq (RPKM) | 6.04 | 11.04 | Very Low |

(211258_s_at and 205015_s_at)

Pearson correlation: 0.93

P-value: 4.27e-35

Note: 2 of the 3 probesets of TGFA (211258_s_at and 205015_s_at) correlate strongly with one another with a r-value of 0.93 while either probesets correlate with 205016_at with a r-value of 0.74 and 0.76, respectively. Further exploring SW480, a duplicate cell line of SW620 derived from the same patient, revealed a similar pattern in all three probes. We conclude that 205106_at is an anomaly that does not follow the pattern of the other two probes. Adding onto the expression level observed in CCLE RNA-Seq data of 6.04, we can conclude a consensus very low expression level of TGFA.

ERBB2 ligand:

| | SW620 | Category |
|--------------------------------|-------|------------|
| Microrarray 216836_s_at | 200 | Very Low |
| Microrarray 210930_s_at | 74 | Background |
| CCLE RNA-Seq (RPKM) | 9.07 | Very Low |

(216836_s_at and 210930_s_at)

Pearson correlation: 0.50

P-value: 2.53e-06

Note: Both probesets of ERBB2 (216836_s_at and 210930_s_at) do not correlate as well with a r-value of 0.5 thus we score them individually and look at them separately. Adding onto the expression level observed in CCLE RNA-Seq data, we can conclude a consensus low expression level of ERBB2.

HBEGF ligand:

| | SW620 | Category |
|------------------------------|-------|------------|
| Microrarray 222076_at | 41 | Background |
| Microrarray 244857_at | 87 | Background |
| Microrarray 38037_at | 189 | Very Low |
| Microrarray 203821_at | 239 | Very Low |
| CCLE RNA-Seq (RPKM) | 1.53 | Very Low |

(222076_at and 203821_at)

Pearson correlation: 0.97

P-value: 5.81e-52

Note: 2 of the 4 probesets of HBEGF (222076_at and 203821_at) correlate strongly with an r-value of 0.97 while 38037_at has a poor correlation with either probesets of 0.02 and 0.02,

respectively, and 203821_at has a poor correlation with either probesets of 0.11 and 0.13, respectively. Surprisingly, 38037_at and 203821_at also have a poor correlation with an r-value of 0.07, suggesting that the two probesets have unique patterns. We conclude that both 38037_at and 203821_at are anomalies that do not behave in line with the other two probes. Thus, 222076_at and 203821_at is assumed to represent the general expression pattern of HBEGF. Adding onto the expression level observed in CCLE RNA-Seq data, we conclude a consensus low expression level of ERBB2.

AREG ligand:

| | SW620 | Category |
|------------------------------|-------|------------|
| Microrarray 205239_at | 97 | Background |
| Microrarray 215564_at | 34 | Background |
| CCLE RN-Seq (RPKM) | 0.103 | Background |

(205239_at and 215564_at)

Pearson correlation: 0.17

P-value: 0.13

Note: Both probesets of AREG (205239_at and 215564_at) do not correlate well with an r-value of 0.17 thus we score them individually and look at them separately. Adding onto the expression level observed in CCLE RNA-Seq data, we can conclude a consensus background expression level of AREG.

EREG ligand:

| | SW620 | Category |
|-------------------------------|-------|------------|
| Microrarray 1569583_at | 59 | Background |
| Microrarray 205767_at | 133 | Background |
| CCLE RNA-Seq (RPKM) | 0.407 | Background |

(1569583_at and 205767_at)

Pearson correlation: 0.81

P-value: 3.77e-19

Discussion: Both probesets of EREG (1569583_at and 205767_at) correlate strongly with an r-value of 0.81. Adding onto the expression level observed in CCLE RNA-Seq data, we can conclude a consensus background expression level of EREG.

BTC ligand:

| | SW620 | Category |
|------------------------------|-------|------------|
| Microrarray 207326_at | 39 | Background |
| Microrarray 241412_at | 16 | Background |
| CCLE RNA-Seq (RPKM) | 0.127 | Background |

(207326_at and 241412_at)

Pearson correlation: 0.87

P-value: 1.50e-25

Note: Both probesets of BTC (207326_at and 241412_at) correlate strongly with an r-value of 0.87. Adding onto the expression level observed in CCLE RNA-Seq data, we conclude a consensus background expression level of BTC.

EGF ligand:

| | SW620 | Category |
|------------------------------|-------|------------|
| Microrarray 206254_at | 26 | Background |

| | | |
|----------------------------|--------|------------|
| CCLE RNA-Seq (RPKM) | 0.0029 | Background |
|----------------------------|--------|------------|

Discussion: EGF has a single probeset with a background expression level. Adding onto the expression level observed in CCLE RNA-Seq data, we can conclude a consensus background expression level of EGF.

EPGN ligand:

| | | |
|----------------------------|--------------|-----------------|
| | SW620 | Category |
| CCLE RNA-Seq (RPKM) | 0 | Background |

Note, there is no available microarray data for EPGN. The CCLE RNA-Seq data showed a level of 0 thus we can conclude a background expression level of EPGN.

Lastly, a good example of a high expression level in CRC cell lines is the marker CDH1 since it is the signature gene expressed by all epithelial cells. In our in-house microarray data, the average expression level of CDH1 is ~6000 while in the CCLE RNA-Seq data lie around 45-60.

Kinetic modeling of EGFR ligand binding, dimerization, endocytosis and recycling

We developed a multi-state time-dependent kinetics model for ligand binding to receptor monomers and dimers, incorporating homo- and hetero-dimerization of ligated and unligated receptors, internalization of ligated receptors via endocytosis and subsequent recycling of receptors to the plasma membrane. The model solves multiple rate equations to determine concentrations of ligated and unligated receptor monomers and dimers, and concentrations of internalized receptors, as a function of time (Supplementary). To match our experiments, the rate constants for ligand binding and unbinding used are based on previous reports for receptor monomers at 37°C (equilibration time scale ~5-10 min) (81, 82). Unligated dimers have the same ligand-binding rate as unligated monomers, whereas singly-ligated dimers have a 14-fold lower binding rate than unligated monomers, as reported from equilibrium measurements at 4°C (8) (details in Supplementary). We do not explicitly model oligomeric or clustered EGFR states, as their rates are unknown. The model assumes the presence of populations of EGFR monomers and dimers (Figure 4a) with higher-order clusters formed by coalesce of monomers and dimers in the plasma membrane. Receptor dimerization rates were chosen to match the relatively fast typical time scales of equilibration of dimer formation in living cells at 37°C (~0.1-1s, see (83)) as well as the fact that we observe few receptor monomers on the cell surface at equilibrium. The unligated-unligated and unligated-ligated receptor dimerization rates are the same, whereas ligated-ligated dimerisation has a 10-fold lower rate as per equilibrium observations at 4°C (8) (details in Supplementary). Under the conditions of our experiments of relatively high EGF concentration where we likely saturate EGFRs at the surface, the rate of internalization is 3-10%/min, dependent on cell line (8, 82). This is lower than that at lower EGF concentrations owing to clathrin endocytosis pathway saturation. Recycling rates of ligand-occupied EGFR are ~10%/min (8), with recycling contributing significantly to the overall receptor distribution only after a pool of endosomal EGFR is accumulated.

The time-dependent kinetic model that we have developed considers: (i) that EGF ligand can bind to both EGFR receptor monomers and dimers, (ii) that ligated EGFR monomers and singly- or doubly-ligated dimers can be internalized via endocytosis, and (iii) that endocytosed receptors can be recycled back to the plasma membrane. EGFR degradation is not included in the model, as the half-life of EGFR degradation after EGF activation is typically of the order of hours(56) and hence has a negligible impact considering the time scale of our measurements (~40 min).

In what follows, we use the following notation: R for receptor monomers, RR for receptor dimers, L for EGF ligand, RL for ligated receptor monomers, RRL for singly-ligated receptor dimers, RRL2 for doubly-ligated receptor dimers, RL^{inside} for endocytosed RL, RRL^{inside} for endocytosed RRL and $RRL2^{\text{inside}}$ for endocytosed RRL2. Our model considers the following reversible reactions for ligand binding and receptor dimerization:

$R + L \rightarrow RL$ with on-rate constant $k_{11,\text{on}}$, off-rate constant $k_{11,\text{off}}$ and equilibrium association constant $K_{11} = k_{11,\text{on}}/k_{11,\text{off}}$;

$RR + L \rightarrow RRL$ with on-rate constant $k_{21,\text{on}}$, off-rate constant $k_{21,\text{off}}$ and equilibrium association constant $K_{21} = k_{21,\text{on}}/k_{21,\text{off}}$;

$RRL + L \rightarrow RRL2$ with on-rate constant $k_{22,\text{on}}$, off-rate constant $k_{22,\text{off}}$ and equilibrium association constant $K_{22} = k_{22,\text{on}}/k_{22,\text{off}}$;

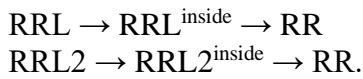
$R + R \rightarrow RR$ with on-rate constant $l_{20,\text{on}}$, off-rate constant $l_{20,\text{off}}$ and equilibrium dimerization constant $L_{20} = l_{20,\text{on}}/l_{20,\text{off}}$;

$RL + R \rightarrow RRL$ with on-rate constant $l_{21,\text{on}}$, off-rate constant $l_{21,\text{off}}$ and equilibrium dimerization constant $L_{21} = l_{21,\text{on}}/l_{21,\text{off}}$;

$RL + RL \rightarrow RRL2$ with on-rate constant $l_{22,\text{on}}$, off-rate constant $l_{22,\text{off}}$ and equilibrium dimerization constant $L_{22} = l_{22,\text{on}}/l_{22,\text{off}}$.

Additionally, we have the following non-reversible endocytosis and recycling reactions:

$RL \rightarrow RL^{\text{inside}} \rightarrow R$



For the last three reactions, the first arrow (endocytosis) is considered to have a rate k_{endoc} and the second arrow (recycling back to the plasma membrane) is considered to have a rate k_{recycle} . We consider only endocytosis of ligated receptors (RL, RRL, RRL2) and, in the first instance, we assume that recycling returns unligated receptors to the plasma membrane. We assume the same endocytosis and recycling rates for the three reactions above.

Considering all the above reactions, it is possible to write a system of simultaneous rate equations as follows:

$$\begin{aligned} \frac{d[\text{RR}]}{dt} &= l_{20,\text{on}} [\text{R}]^2 - l_{20,\text{off}} [\text{RR}] - k_{21,\text{on}} [\text{RR}][\text{L}] + k_{21,\text{off}} [\text{RRL}] + k_{\text{recycle}} [\text{RRL}^{\text{inside}}] + k_{\text{recycle}} [\text{RRL2}^{\text{inside}}], \\ \frac{d[\text{RL}]}{dt} &= k_{11,\text{on}} [\text{R}][\text{L}] - k_{11,\text{off}} [\text{RL}] - k_{\text{endoc}} [\text{RL}] - l_{21,\text{on}} [\text{RL}][\text{R}] + l_{21,\text{off}} [\text{RRL}] - l_{22,\text{on}} [\text{RL}]^2 + \\ &\quad l_{22,\text{off}} [\text{RRL2}], \\ \frac{d[\text{RRL}]}{dt} &= k_{21,\text{on}} [\text{RR}][\text{L}] - k_{21,\text{off}} [\text{RRL}] - k_{\text{endoc}} [\text{RRL}] + l_{21,\text{on}} [\text{RL}][\text{R}] - l_{21,\text{off}} [\text{RRL}] - k_{22,\text{on}} [\text{RRL}][\text{L}] + \\ &\quad k_{22,\text{off}} [\text{RRL2}], \\ \frac{d[\text{RRL2}]}{dt} &= k_{22,\text{on}} [\text{RRL}][\text{L}] - k_{22,\text{off}} [\text{RRL2}] - k_{\text{endoc}} [\text{RRL2}] + l_{22,\text{on}} [\text{RL}]^2 - l_{22,\text{off}} [\text{RRL2}], \\ \frac{d[\text{RL}^{\text{inside}}]}{dt} &= k_{\text{endoc}} [\text{RL}] - k_{\text{recycle}} [\text{RL}^{\text{inside}}], \\ \frac{d[\text{RRL}^{\text{inside}}]}{dt} &= k_{\text{endoc}} [\text{RRL}] - k_{\text{recycle}} [\text{RRL}^{\text{inside}}], \\ \frac{d[\text{RRL2}^{\text{inside}}]}{dt} &= k_{\text{endoc}} [\text{RRL2}] - k_{\text{recycle}} [\text{RRL2}^{\text{inside}}], \\ [\text{R}] &= \text{R}_{\text{total}} - ([\text{RL}] + [\text{RR}] + [\text{RRL}] + [\text{RRL2}] + [\text{RL}^{\text{inside}}] + [\text{RRL}^{\text{inside}}] + [\text{RRL2}^{\text{inside}}]). \end{aligned}$$

Here t is time and the square brackets indicate concentration of reactant/product, with all concentrations being functions of time, and all rates defined as above. R_{total} is the total concentration of receptors (including both receptors on the surface and internalised), i.e., the total number of receptor molecules per cell. This value is set to 200,000-400,000 molecules/cell (depending on the model parameters used) to match our observations of approximately 200,000 receptors on the cell surface in experiments.

In order to solve the system of equations we consider the following initial conditions: $[\text{RL}](t=0) = [\text{RRL}](t=0) = [\text{RRL2}](t=0) = [\text{RL}^{\text{inside}}](t=0) = [\text{RRL}^{\text{inside}}](t=0) = [\text{RRL2}^{\text{inside}}](t=0) = 0$, i.e., that all ligated and internalised components are zero at $t=0$, and we set the initial concentrations of unligated receptor monomers and dimers to certain fractions of R_{total} , typically ~5% monomer fraction and ~95% dimer fraction, in agreement with the fact that we observe mostly clusters of receptors and hardly any monomers in our experiments. The ligand concentration, $[\text{L}]$, used is that in our experiments: 100 ng/ml ~ 15.6 nM.

The rate constants for monomer ligand binding/unbinding are given values $k_{11,\text{on}} = 10^6 \text{M}^{-1} \text{s}^{-1}$ and $k_{11,\text{off}} = 10^{-3} \text{s}^{-1}$, so that the equilibrium association constant is $K_{11} = 10^9 \text{M}^{-1}$. These rate constants are similar to those previously reported for EGFR monomers(82) and ensure that the time scale of equilibration of receptor binding is ~5-10 min, in agreement with measurements reported in live cells at 37°C (81, 82). We assume that the ligand binding/unbinding rate constants for unligated receptor dimers are the same as for unligated monomers, i.e., $k_{21,\text{on}} = k_{11,\text{on}}$ and $k_{21,\text{off}} = k_{11,\text{off}}$ (hence $K_{21} = K_{11}$). This assumption is motivated by the fact that the equilibrium association constants for R and RR binding to ligand for EGFR have been reported to be approximately the same, i.e., $K_{21} \approx K_{11}$, as obtained from measurements in cells at 4°C(8). The same study reported that the equilibrium association constant for ligand binding to singly-ligated receptor dimers is ~14 times lower than that for unligated monomers/dimers, i.e., $K_{22} \approx K_{11}/14$. To include this reported lower affinity of ligand for singly-ligated receptors, we choose on/off-rate constants for ligand binding to RRL of $k_{22,\text{on}} = k_{11,\text{on}}/7$ and $k_{22,\text{off}} = 2 \times k_{11,\text{off}}$. Note that these conditions imply that there is negative cooperativity of EGFRs in ligand binding, as $K_{22} < K_{11}/4$.

As for receptor dimerization, equilibration is achieved in shorter times, of the order of ~ 0.1 -1s, as measured for G-protein-coupled receptors (GPCRs) in living cells at 37°C (83). For our model, we choose an equilibrium dimerization constant $L_{20} = 10^{-3}(\text{molecules/cell})^{-1}$ in units of 2D concentration (with 1 receptor molecule per μm^2 corresponding to approximately 3,000 receptors/cell), 10 times higher than the value measured for GPCRs. We use $l_{20,on} = 10^{-4}(\text{molecules/cell})^{-1}\text{s}^{-1}$ and $l_{20,off} = 10^{-1}\text{s}^{-1}$ to guarantee that the time scale of dimer formation equilibration is correct and to ensure that there are very few monomers on the cell surface at equilibrium ($\sim 5\%$ monomers, $\sim 95\%$ dimers), in agreement with our own experimental observations. For the dimerization rate of RL and R, we use $l_{21,on} = l_{20,on}$ and $l_{21,off} = l_{20,off}$ as the respective equilibrium dimerization constants reported from measurements in cells at 4°C are very similar ($L_{21} \approx L_{20}$) (8). As the dimerization rate L_{22} for RL+RL was reported to be ~ 10 times lower than L_{20} in the same study, we choose as model parameters $l_{22,on} = l_{20,on}/5$ and $l_{22,off} = 2 \times l_{20,off}$.

We set the rate of endocytosis of ligated receptors in our model to $k_{endoc} = 6\%/min = 0.06/60\text{s}^{-1}$, in agreement with previous reports of EGFR endocytosis rates in living cells at 37°C in the presence of high EGF concentrations similar to that in our experiments, which are in the range 3 – 10 %/min (8, 82). EGFR endocytosis rates at low ligand concentrations (near physiological levels [EGF] $\sim 1\text{ng/ml}$) are typically in the range 15 – 30 %/min. At higher EGF concentrations ($\sim 100\text{ng/ml}$) and high receptor numbers (as in our experiments), the clathrin-endocytosis pathway saturates, and the endocytosis rate is lower (3 – 10 %/min). Endocytosis rates in the absence of EGF ligand are greatly decelerated with respect to the above rates (8). The recycling rate is set to $k_{recycle} = 10\%/min = 0.1/60\text{s}^{-1}$ (8).

Using all the above parameter values, we solve the above system of differential equations in order to find [R], [RL], [RR], [RRL], [RRL2], $[\text{RL}^{\text{inside}}]$, $[\text{RRL}^{\text{inside}}]$ and $[\text{RRL2}^{\text{inside}}]$ as a function of time. Additionally, we calculate the fractional saturation on the cell surface, Y^{surface} , equal to the ratio of EGF to EGFR molecules (EGF:EGFR ratio) on the plasma membrane. This is given by:

$$Y^{\text{surface}} = \frac{[R_{\text{bound}}]^{\text{surface}}}{[R_{\text{bound}}]^{\text{surface}} + [R_{\text{unbound}}]^{\text{surface}}} = \frac{[\text{RL}] + [\text{RRL}]/2 + [\text{RRL2}]}{[\text{R}] + [\text{RL}] + [\text{RR}] + [\text{RRL}] + [\text{RRL2}]} .$$

Here, we account for the fact that all concentrations involving receptors in the model are obtained as numbers of receptor molecules per cell. The value of the EGFR:EGF ratio obtained from our experimental measurements is ~ 4 on average (and ~ 2 as a modal peak value), which would correspond to a Y^{surface} value in our model of ~ 0.25 (and peak value ~ 0.5). The calculated variables as a function of time for the above-mentioned parameters are shown in Figure 4a in the main text. We use $R_{\text{total}} = 310,000$ molecules/cell, which is the value that results in a total number of receptor molecules on the cell surface (excluding internalised receptors) at equilibrium of 200,000, in agreement with our observations. We find that the fractional saturation at the cell surface is $Y^{\text{surface}} \sim 0.66$, i.e., the EGFR:EGF ratio predicted by the model is ~ 1.5 .

The results for Y^{surface} (at equilibrium) do not change significantly upon various changes of the model parameters. Changing the value of R_{total} by $\pm 100,000$ receptors/cell only alters the result by $< 2\%$. Increasing the endocytosis rate to 10%/min yields $Y^{\text{surface}} 0.62$ and decreasing it to 3%/min yields $Y^{\text{surface}} 0.72$. Increasing the recycling rate up to 40%/min does not change the value of Y^{surface} at equilibrium, decreasing it to 0 results in $Y^{\text{surface}} 0.83$ and a largely reduced number of receptors at the cell surface ($\sim 30,000$) after 40 minutes. Increasing or decreasing all ligand binding on-rate constants by a factor of 2 results in moderately increased or decreased values at equilibrium, $Y^{\text{surface}} 0.77$ or $Y^{\text{surface}} 0.55$, respectively. Increasing or decreasing all ligand binding off-rate constants by a factor of 2 results in moderately decreased or increased values, $Y^{\text{surface}} 0.61$ or $Y^{\text{surface}} 0.70$, respectively. Increasing or decreasing all receptor dimerization on-rate constants by a factor of 2 changes the result only by $< 3\%$. Changing the factors in $k_{22,on}$ and $k_{22,off}$ that guarantee that $K_{22} = K_{11}/14$, to go from $k_{22,on} = k_{11,on}/7$ and $k_{22,off} = 2 \times k_{11,off}$ to the extremes $k_{22,on} = k_{11,on}/14$, $k_{22,off} = k_{11,off}$ or $k_{22,on} = k_{11,on}$, $k_{22,off} = 14 \times k_{11,off}$ changes the result by at most 3%. Changing the factors that

guarantee that $L_{22} = L_{20}/10$ to the extremes $l_{22,on} = l_{20,on}/10$, $l_{22,off} = l_{20,off}$ and $l_{22,on} = l_{20,on}$, $l_{22,off} = 10 \times l_{20,off}$, does not change the result at all. Reducing all dimerization on/off-rate constants by a factor of 100 (which increases the dimerization equilibration time from ~1s to ~1min) only increases $Y^{surface}$ to 0.68 (by 3%). Changing the initial fractions of receptor monomers and dimers at $t=0$ does not change the results as the equilibration time of dimerization is short (~1s).

Setting the binding on-rate constant for singly-ligated dimers to zero ($k_{22,on} = 0$), i.e. assuming extreme negative cooperativity, the result remains the same ($Y^{surface} 0.66$). Setting the binding on-rate constant for unligated dimers to zero ($k_{21,on} = 0$) makes a significant difference and results in $Y^{surface} 0.24$, i.e., in an EGFR:EGF ratio at equilibrium on the cell surface of ~4 (see Figure 4b in the main text). This is the case regardless of whether $k_{22,on}$ is also set to zero or not, i.e., this result is consistent also with extreme preferential ligand binding to monomers (ligand can bind to receptor monomers but not to dimers). Setting the binding on-rate constant for receptor monomers to zero ($k_{11,on} = 0$), i.e., assuming extreme preferential ligand binding to dimers, yields $Y^{surface} 0.63$. In the case of positive cooperativity, setting $k_{22,on} = k_{11,on}$ and $k_{22,off} = k_{11,off}$, the result increases to $Y^{surface} 0.69$. Considering more significant positive cooperativity with $k_{22,on} = 10k_{11,on}$ and $k_{22,off} = k_{11,off}$, we obtain an even higher value, $Y^{surface} 0.82$. Hence, positive cooperativity leads to higher values of $Y^{surface}$, while negative cooperativity leads to lower values. Hence, the latter agrees better with our experimental results that correspond to an EGFR:EGF ratio ~4 on average (i.e., to $Y^{surface} 1/4$). Model predictions in the case of preferential ligand binding to monomers would agree with experimental observations. We also tried setting some of the dimerization rate constants to zero as follows. Assuming that R monomers do not dimerize to form RR dimers ($l_{20,on} = 0$), we obtain $Y^{surface} 0.49$ and $Y^{surface} 0.69$ if we also set the off-rate constant to zero ($l_{20,off} = 0$). Assuming that RL and R do not dimerize to form RRL ($l_{21,on} = 0$), we obtain $Y^{surface} 0.92$ and $Y^{surface} 0.69$ if we also set the off-rate constant to zero ($l_{21,off} = 0$). Hence, a decreased hetero-dimerization rate constant (ligated-unligated) leads to model predictions that are further from our experimental observations. Assuming that RL complexes do not dimerize to form RRL2 ($l_{22,on} = 0$), we obtain $Y^{surface} 0.53$ and $Y^{surface} 0.68$ if we also set the off-rate to zero ($l_{22,off} = 0$). Setting both R and RL homo-dimerization rate constants (unligated-unligated and ligated-ligated) to zero ($l_{20,on} = 0$ and $l_{22,on} = 0$), the model yields $Y^{surface} 0.47$. Hence, a reduced homo-dimerization on-rate constant for unligated and/or ligated monomers (i.e., a reduced $l_{20,on}$ and/or a reduced $l_{22,on}$) yields model results that are closer to our experimental observations (a lower $Y^{surface}$ value).

We also tested in our model ligand binding and dimerization rate constants that result in the same equilibrium association constants as those reported from measurements in cells at 4°C, i.e., $K_{11} \approx 5 \times 10^9 M^{-1}$, $K_{21} \approx K_{11}$, $K_{22} \approx K_{11}/14$, $L_{20} \approx 2 \times 10^{-5} (molecs/cell)^{-1}$, $L_{21} \approx L_{20}$ and $L_{22} \approx L_{20}/10$ (8). In this case, we set the model parameters to $R_{total} = 310000$ molecules/cell, 5% and 95% initial fractions of monomers and dimers respectively, $[L] = 15.6 \times 10^{-9} M$, $k_{endoc} = 0.06/60 s^{-1}$, $k_{recycle} = 0.1/60 s^{-1}$ (up to here all parameters are the same as previously), and $k_{11,on} = 10^7 M^{-1} s^{-1}$, $k_{11,off} = 2 \times 10^{-3} s^{-1}$, $k_{21,on} = k_{11,on}$, $k_{21,off} = k_{11,off}$, $k_{22,on} = k_{11,on}/7$ and $k_{22,off} = 2 \times k_{11,off}$, $l_{20,on} \approx 2 \times 10^{-5} (molecs/cell)^{-1} s^{-1}$ and $l_{20,off} = 1 s^{-1}$, $l_{21,on} = l_{20,on}$, $l_{21,off} = l_{20,off}$, $l_{22,on} = l_{20,on}/5$ and $l_{22,off} = 2 \times l_{20,off}$. Using these parameters, the value of the surface fractional saturation (EGF:EGFR ratio) is $Y^{surface} 0.96$ (see Figure 4c in the main text). The result remains the same if all binding on/off-rate constants are multiplied or divided by 10, or if all dimerization on/off-rate constants are multiplied or divided by 10, keeping the equilibrium association constants the same. This value of $Y^{surface} 0.96$ close to 1 at our ligand concentration, as well as values obtained at ligand concentrations in the range 10^{-11} - $10^{-6} M$ (Figure 4c, main text) are all consistent with results at 4°C from alternative models based on equilibrium equations (that do not include time

dependence) (8), proving the validity of our model. It is important to note that the on/off-rate constants can have a strong temperature dependence and that results measured at 4°C can differ significantly (up to a factor of 10-100) from measurements at 37°C (55).

In conclusion, the value we obtain experimentally for the EGFR:EGF ratio in living cells at 37°C agrees better with model predictions in the cases in which there is negative cooperativity for ligand binding and preferential ligand binding to monomers or reduced homo-dimerization on-rate constants (for unligated-unligated and ligated-ligated dimerization).

Additionally, we considered a model in which ligated receptors are recycled back to the plasma membrane ligated, as opposed to unligated. In this case, the system of rate equations that we solve is the following:

$$\begin{aligned}\frac{d[RR]}{dt} &= l_{20,on} [R]^2 - l_{20,off} [RR] - k_{21,on}[RR][L] + k_{21,off}[RRL], \\ \frac{d[RL]}{dt} &= k_{11,on}[R][L] - k_{11,off}[RL] - k_{endoc}[RL] - l_{21,on}[RL][R] + l_{21,off}[RRL] - l_{22,on} [RL]^2 + \\ &\quad l_{22,off}[RRL2] + k_{recycle}[RL^{inside}], \\ \frac{d[RRL]}{dt} &= k_{21,on}[RR][L] - k_{21,off}[RRL] - k_{endoc}[RRL] + l_{21,on}[RL][R] - l_{21,off}[RRL] - k_{22,on}[RRL][L] + \\ &\quad k_{22,off}[RRL2] + k_{recycle}[RRL^{inside}], \\ \frac{d[RRL2]}{dt} &= k_{22,on}[RRL][L] - k_{22,off}[RRL2] - k_{endoc}[RRL2] + l_{22,on} [RL]^2 - l_{22,off}[RRL2] + \\ &\quad k_{recycle}[RRL2^{inside}], \\ \frac{d[RL^{inside}]}{dt} &= k_{endoc}[RL] - k_{recycle}[RL^{inside}], \\ \frac{d[RRL^{inside}]}{dt} &= k_{endoc}[RRL] - k_{recycle}[RRL^{inside}], \\ \frac{d[RRL2^{inside}]}{dt} &= k_{endoc}[RRL2] - k_{recycle}[RRL2^{inside}], \\ [R] &= R_{total} - ([RL] + [RR] + [RRL] + [RRL2] + [RL^{inside}] + [RRL^{inside}] + [RRL2^{inside}]).\end{aligned}$$

The solution we obtain with the original set of parameters ($R_{total} = 310000$ moles/cell, 5% and 95% initial fractions of monomers and dimers respectively, $[L] = 15.6 \times 10^{-9}M$, $k_{endoc} = 0.06/60 s^{-1}$, $k_{recycle} = 0.1/60 s^{-1}$, $k_{11,on} = 10^6 M^{-1}s^{-1}$, $k_{11,off} = 10^{-3}s^{-1}$, $k_{21,on} = k_{11,on}$, $k_{21,off} = k_{11,off}$, $k_{22,on} = k_{11,on}/7$ and $k_{22,off} = 2 \times k_{11,off}$, $l_{20,on} \approx 10^{-4}(moles/cell)^{-1}s^{-1}$, $l_{20,off} = 0.1s^{-1}$, $l_{21,on} = l_{20,on}$, $l_{21,off} = l_{20,off}$, $l_{22,on} = l_{20,on}/5$ and $l_{22,off} = 2 \times l_{20,off}$) is $Y^{surface} 0.81$. Similarly, to what occurred for the previously mentioned model predictions for experiments at 37°C, the value of the surface fractional saturation decreases significantly when setting $k_{21,on}$ to zero, to $Y^{surface} 0.36$. Variations upon changes of parameters are very similar to those for the previous model at 37°C. Results from this second model are somewhat further from our experimental observations but the conclusions from above remain valid for both types of recycling processes considered (ligated receptors being endocytosed and recycled back to the plasma membrane unligated or ligated).

Considering our model predictions, we can account for our data by a combination of negative cooperativity of binding and decreased affinity of ligand for dimers. Reduced homo-dimerization on-rates might also play a role, as they result in lower $Y^{surface}$ values and hence in higher EGFR:EGF ratios, closer to our measured data (Figure 4d, Figure S10, Supplementary). These predictions could be consistent with initial EGF binding to monomeric EGFR to generate an activated state predisposed to dimerize with unligated EGFR. Figure 4e (solid green line) validates our model by showing that it can reproduce previously published (22) equilibrium results measured at 4°C as a function of ligand concentration.

Supplementary Figures

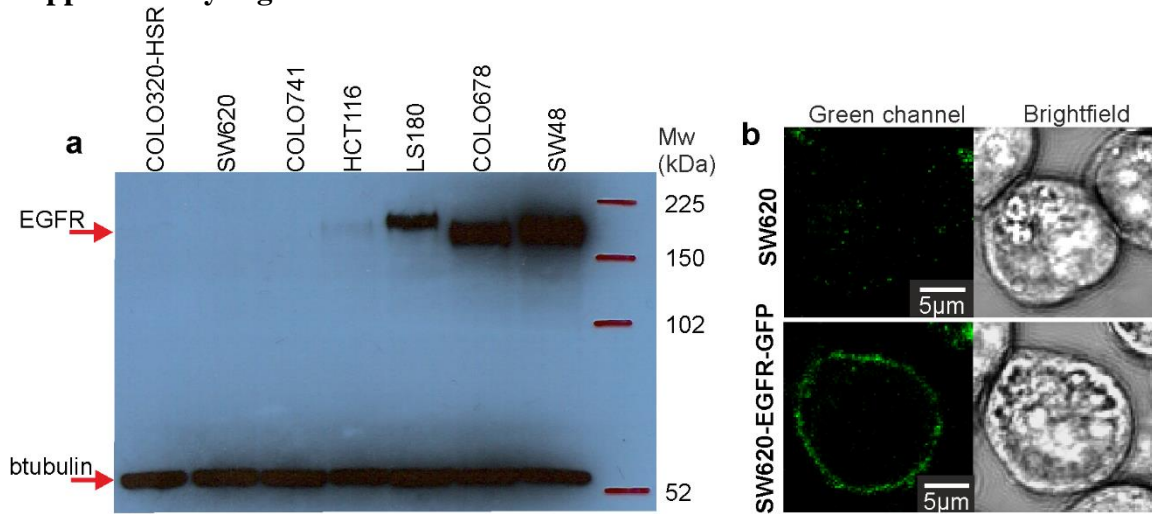


Figure S1: (a) SDS-PAGE for candidate colon carcinoma cell lines, indicating that SW620 COLO320-HSR cells have negligible endogenous EGFR expression compared to positive controls HCT116, LS180, COLO678 and SW48 cells. (b) Parental SW620 shows minimal autofluorescence (upper left), while stably transfected SW620-EGFR-GFP (lower left) show plasma membrane localization of EGFR-GFP from confocal imaging of cells focusing at mid-cell-height (soon after adhering to the coverslip surface).

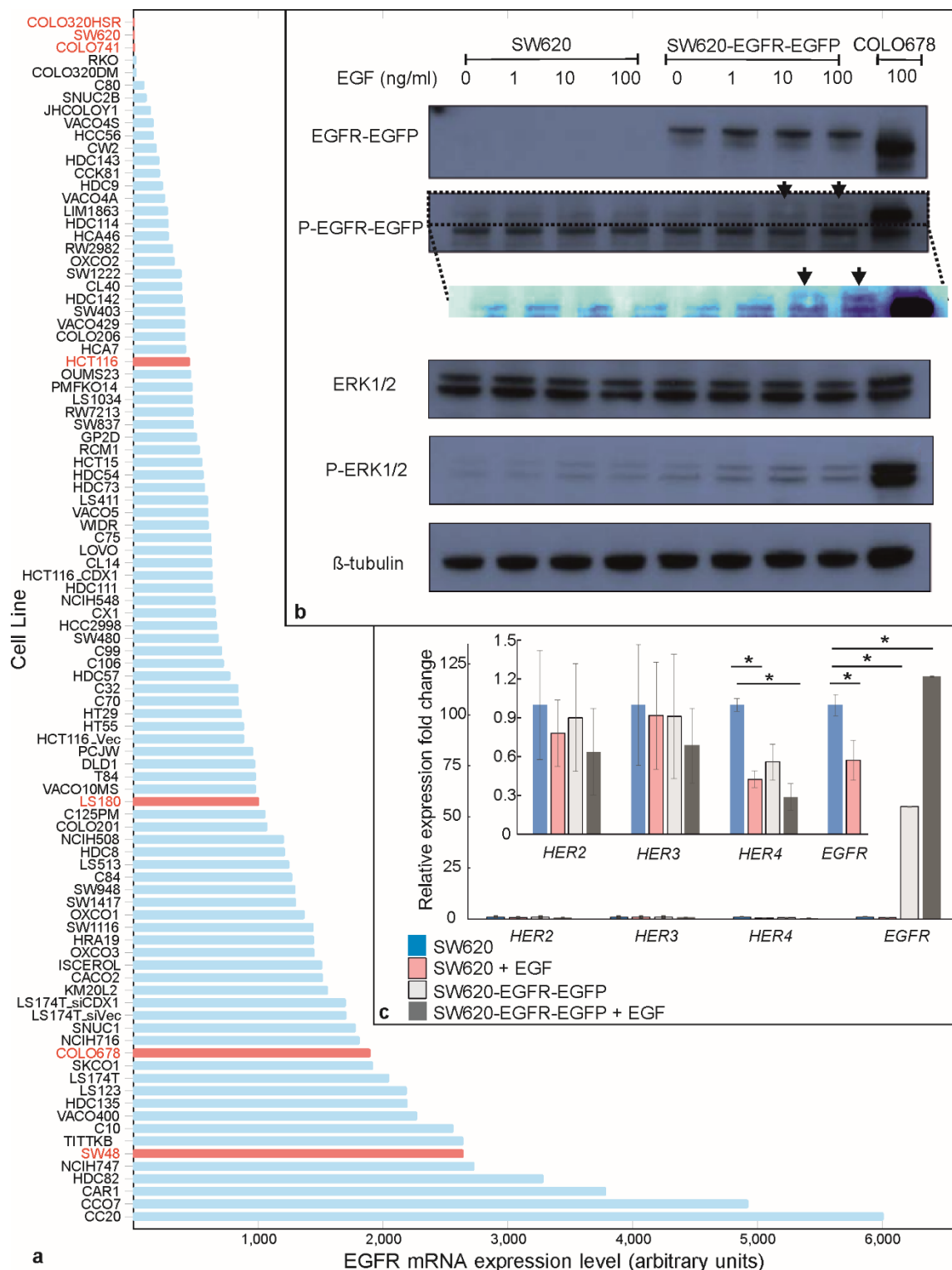


Figure S2: EGFR expression levels. (a). The mRNA expression levels were quantified for a colon cancer-cell line panel using Affymetrix U133+2 mRNA microarray data. Measurements indicated three candidate cell lines, SW620, COLO320HSR and COLO741 (labeled in red, top of panel), as having very low or absent levels of native EGFR expression, as tested in subsequent western blot analysis in comparison to EGFR-expressing cell lines as positive controls (indicated as red columns, middle and bottom of panel). A further four positive controls with medium to high levels (HCT116, LS180, COLO678; indicated as red columns, middle and bottom of panel) can be seen. (b). SDS-PAGE performed on protein extracts obtained from SW620 wild type and SW620-EGFR-GFP cells before and after EGF treatment. COLO680 is used as a positive control. SW620 extracts do not have levels of EGFR detectable by SDS-PAGE, unlike SW620-EGFR-GFP, confirming successful transfection and expression of the GFP-tagged EGFR. EGF treatment of the transfected line results at concentrations of 10ng/ml or above results in detectable levels of phosphorylated EGFR (black arrows and inset with

enhanced display contrast). EGF treatment of SW620-EGFR-GFP results in increased levels of phosphorylated ERK1/2 kinases, downstream players of the EGFR/ERK pathway, confirming the kinase activity of the receptor. (c). Fold expression change of HER2, HER3, HER4 and EGFR relative to the PQLC2 house-keeping gene in SW620 and SW620-EGFR-GFP cells with or without EGF treatment. The relative fold expression change was calculated based on the $\Delta\Delta C_t$ method. The results represent the mean values and standard errors of four experiments on two biological replicates. *=Student t-test $P<0.05$.

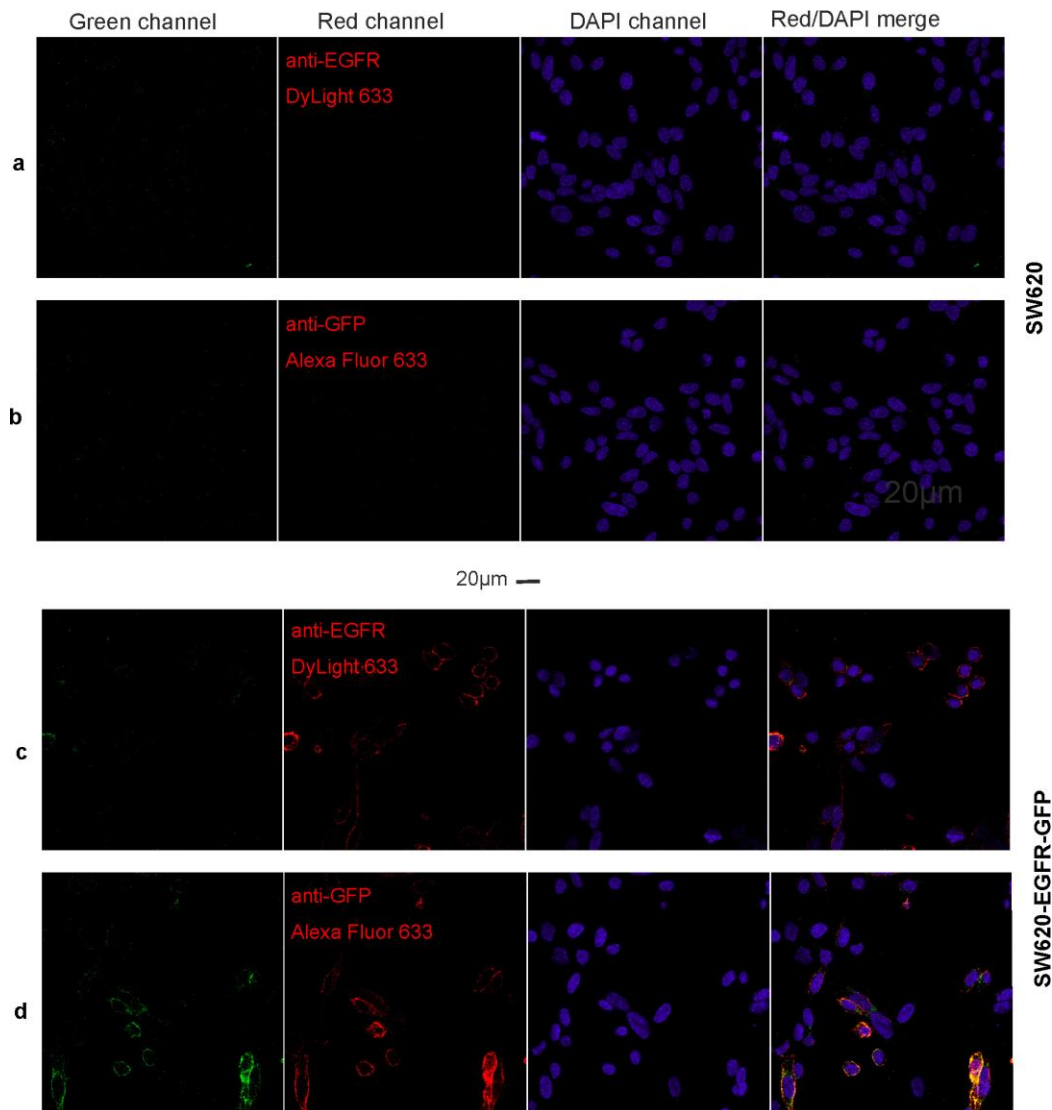


Figure S3: Confocal microscopy images of fixed cells using GFP, anti-GFP immunofluorescence, and DAPI staining: (a,b) non-GFP background cell line SW620; (c,d) SW620-EGFR-GFP.

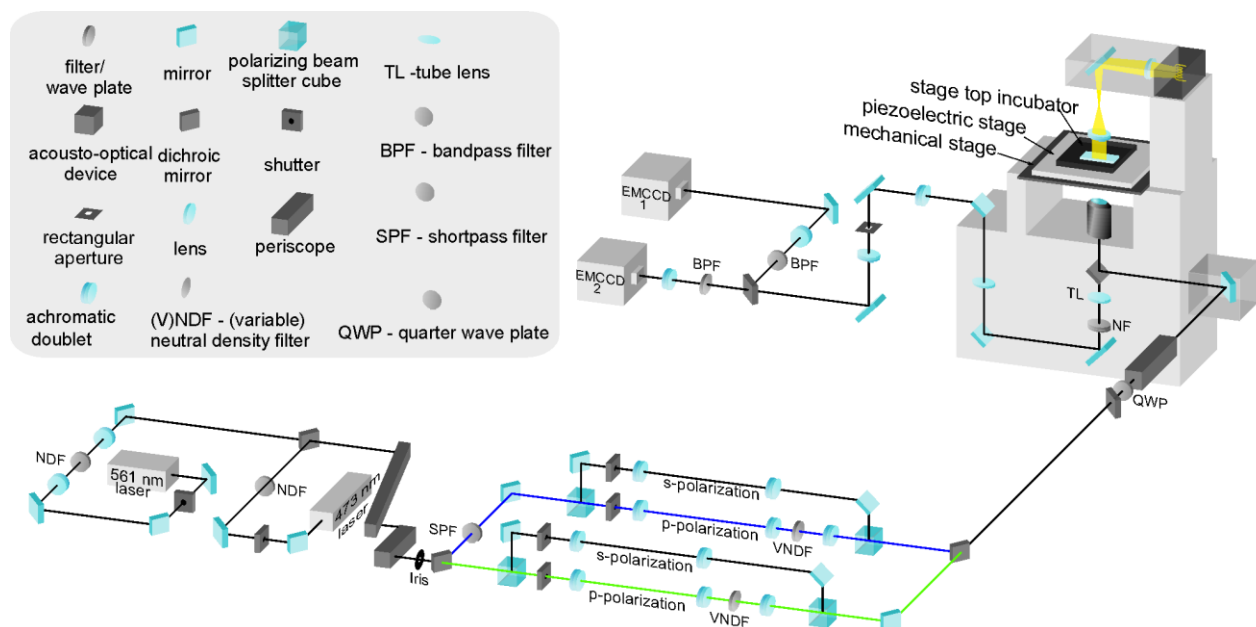


Figure S4: optical-path diagram of bespoke single-molecule TIRF microscope.

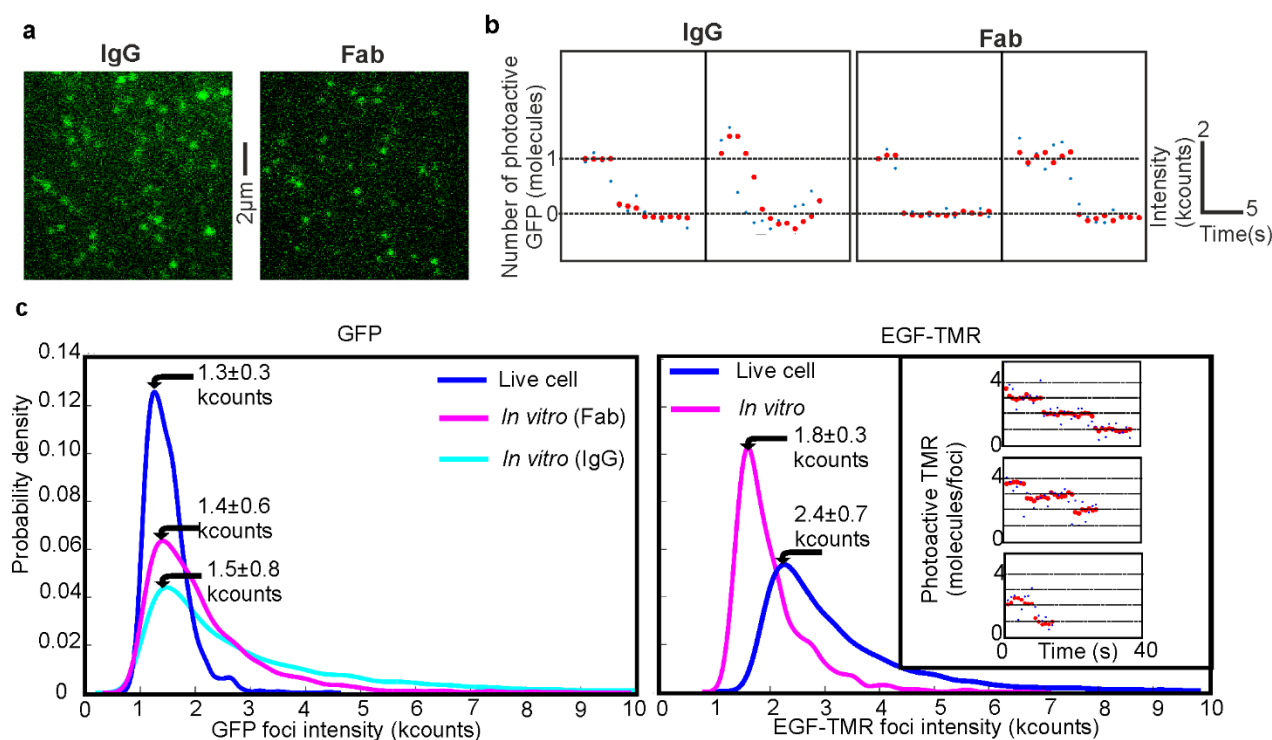


Figure S5: Characterization of unitary fluorophore brightness values. (a) TIRF of GFP in vitro using IgG and Fab conjugation. (b) Step-wise photobleaching showing raw data (blue) and output data of an edge-preserving Chung-Kennedy filter (red) (43, 44) given in kcounts (i.e. counts on detector times 10^3). (c) Kernel density estimation (45) distributions of fluorescent foci intensity values measured in kcounts. **Left panel:** measurements for single GFP in a live cell at the end of the photobleach, before EGF is added, are compared with in vitro Fab and whole IgG data. Arrows indicate mean and s.e.m. **Right panel:** TMR single molecule data for EGF-TMR in vitro and in a live cell at the end of the photobleach, post EGF binding and taken from colocalized EGF-EGFR foci. Arrows indicate mean and s.e.m. **Inset:** live cell EGF-TMR photobleach steps after EGF has been added, taken from colocalized EGF-EGFR foci, with raw data traces (blue) and Chung-Kennedy-filtered traces (red). The difference between peak in vitro and in vivo foci intensity is consistent with in vivo GFP being marginally further (ca. 10-20 nm) from the coverslip surface in the TIRF evanescent field.

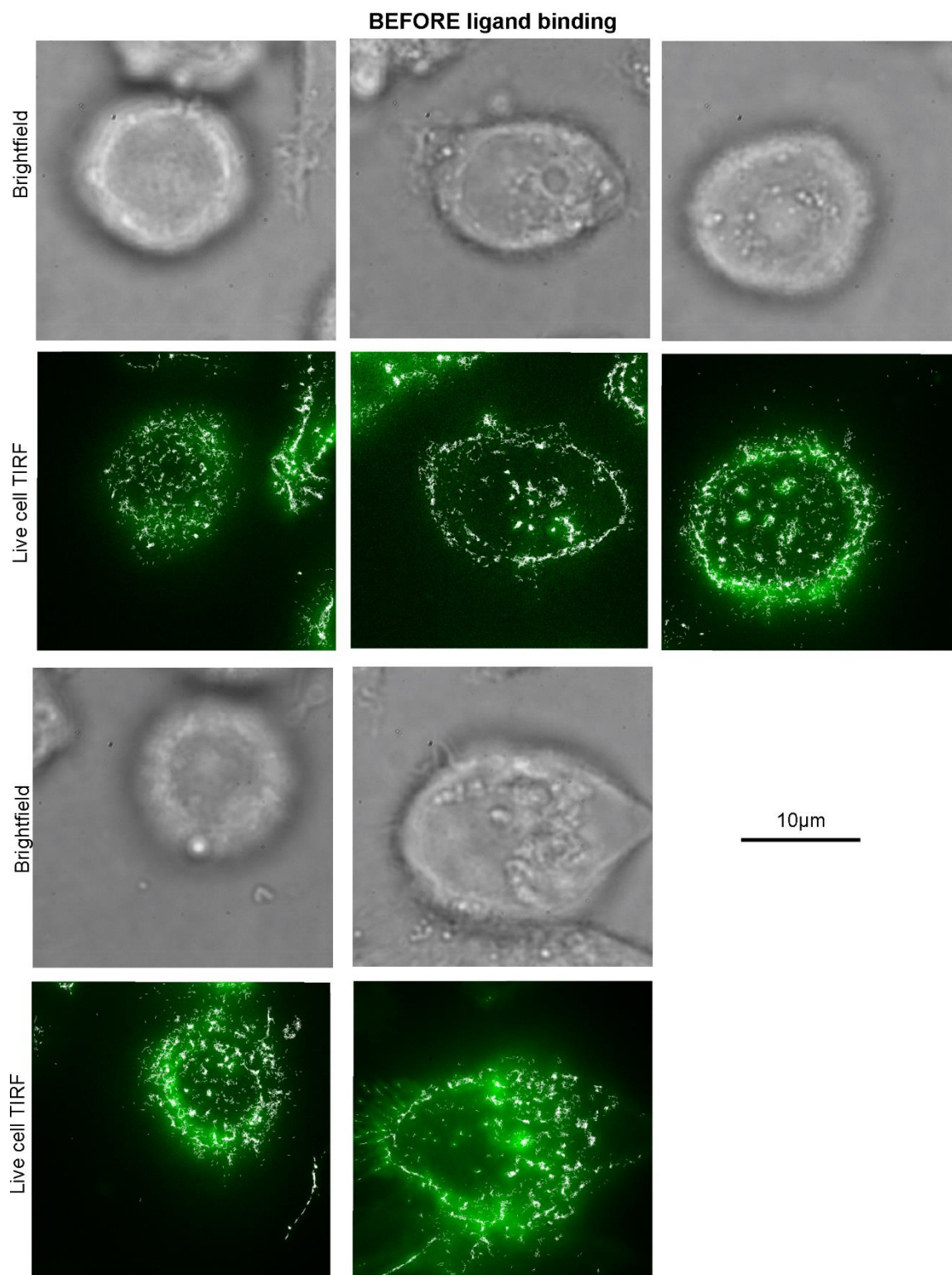


Figure S6: More examples of cells before addition of EGF ligand. Brightfield images (grey) and TIRF images (green) shown with overlaid fluorescent foci tracking output (white).

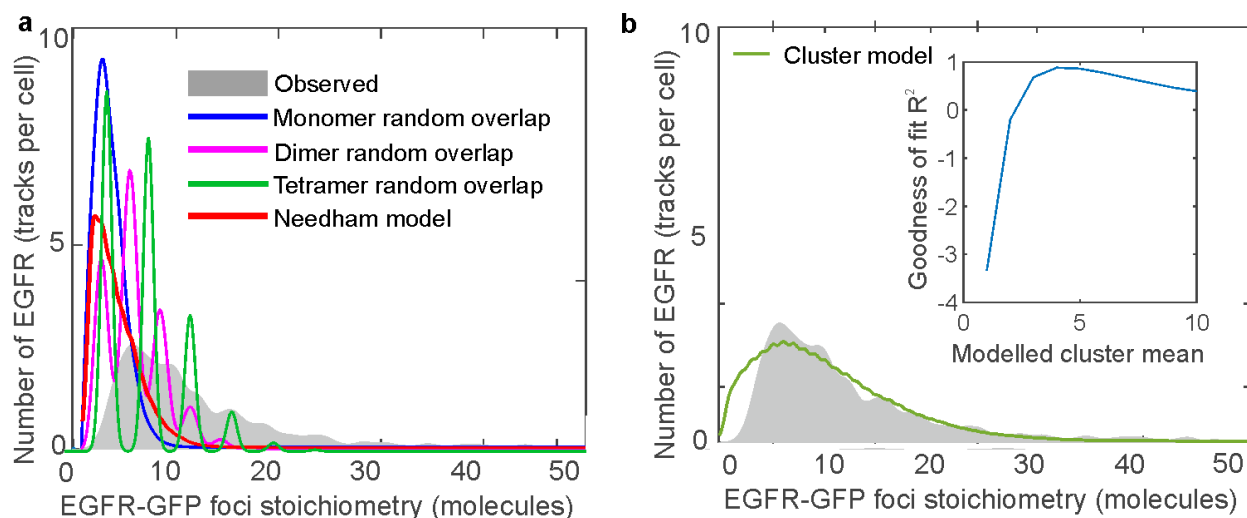


Figure S7 Random foci overlap model. **a:** Model for the random overlap of EGFR molecules/cluster on the cell surface based on chance colocalization. The predicted cluster stoichiometry distributions are shown for the random overlap of EGFR monomers (blue), dimers (magenta), tetramer (green) and for a mixed model assuming 51.3% 1-mer, 21.3% 2-mer, 10.3% 3-mer, 5.3% 4-mer and 4.1% 5-mer per EGFR cluster) suggested by a previous single-molecule study (red) by Needham et al. (47). Our own experimental stoichiometry distribution (grey) is in poor agreement with these models ($R^2 < 0$). **b:** Predictions (green) using a cluster model with expected average value of 4 molecules per EGFR cluster, together with experimental data (grey). A regression fit can account for ca. 90% of the experimental variance ($R^2 = 0.88$). R^2 as a function of average model cluster size is shown in the insert.

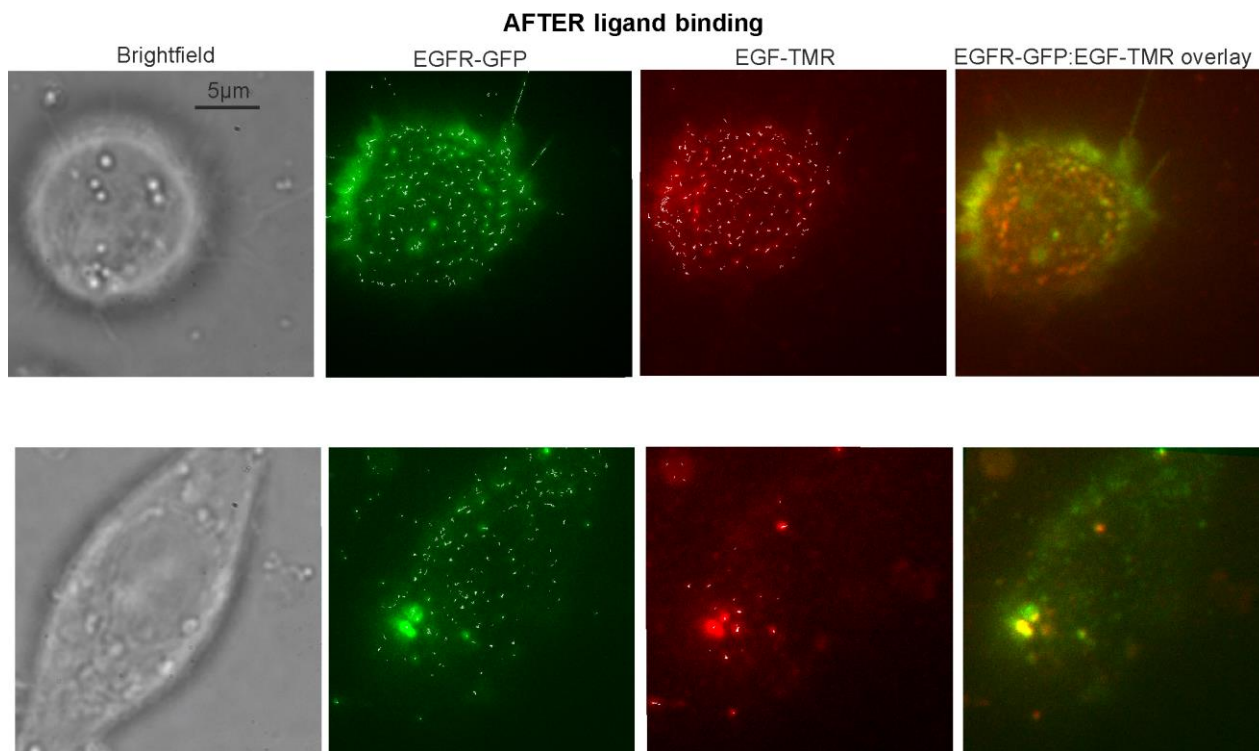


Figure S8: Colocalization of EGFR and EGF foci after addition of EGF. Two examples (top and bottom) of cells taken ~10 min after addition of EGF. Shown from left to right are: brightfield images (grey), green channel with EGFR-GFP localizations (green), red channel with EGF-TMR localizations (red), and overlay of green and red channels, with yellow indicating regions of high colocalization.

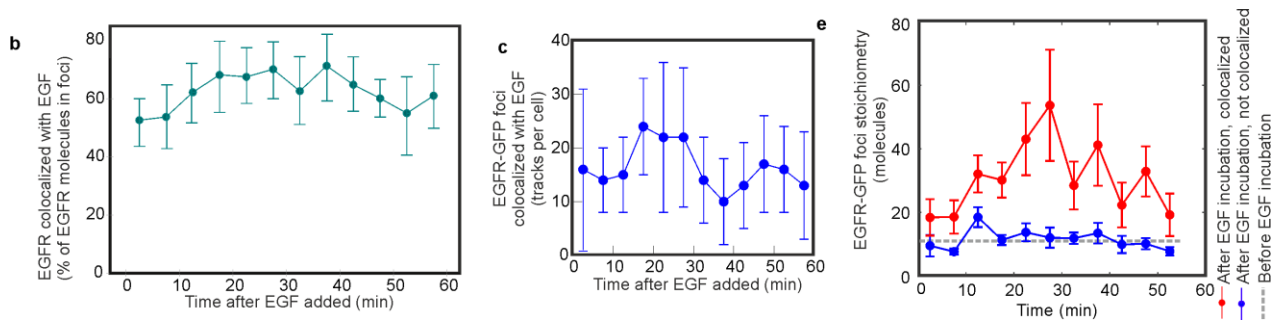
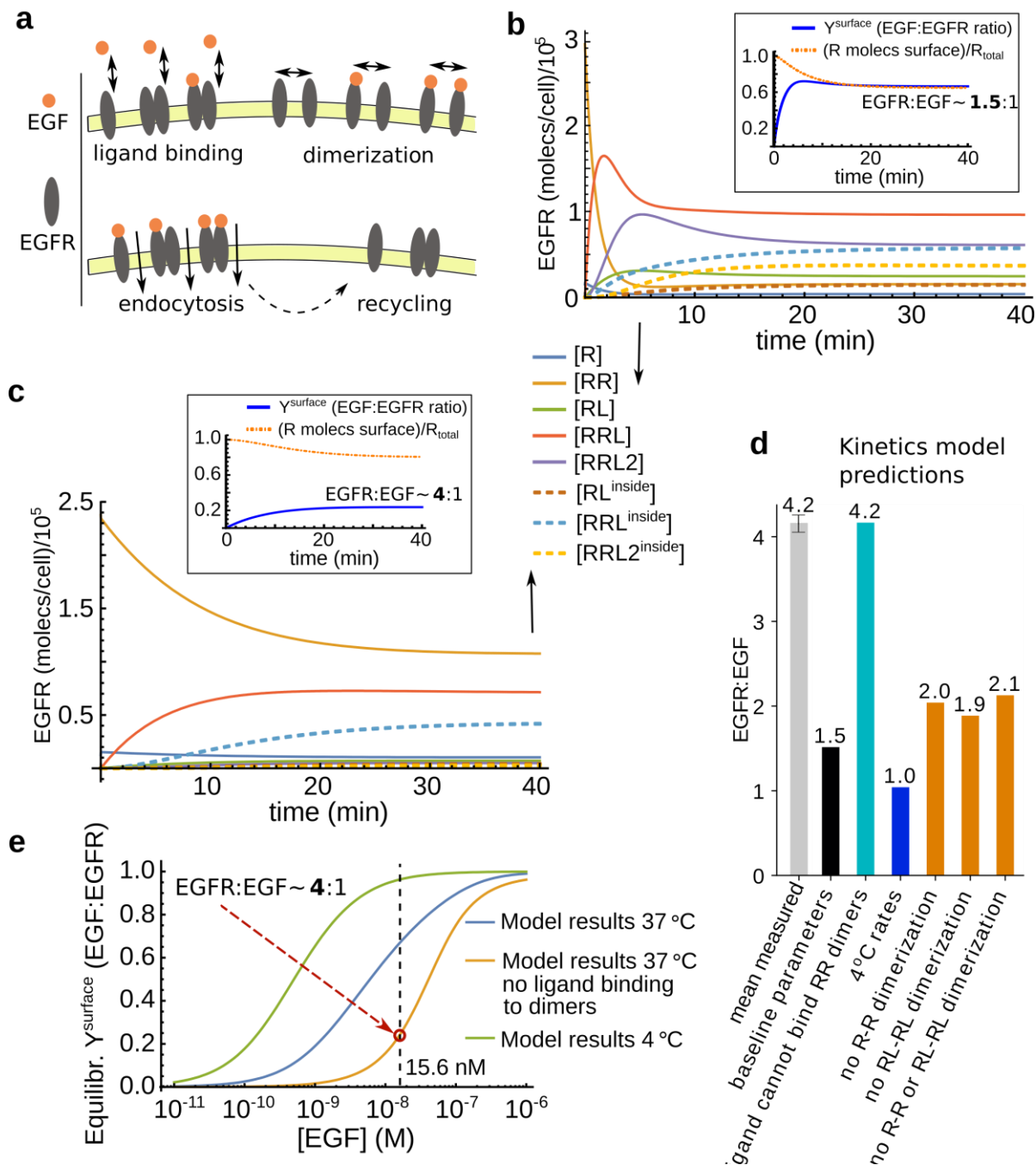
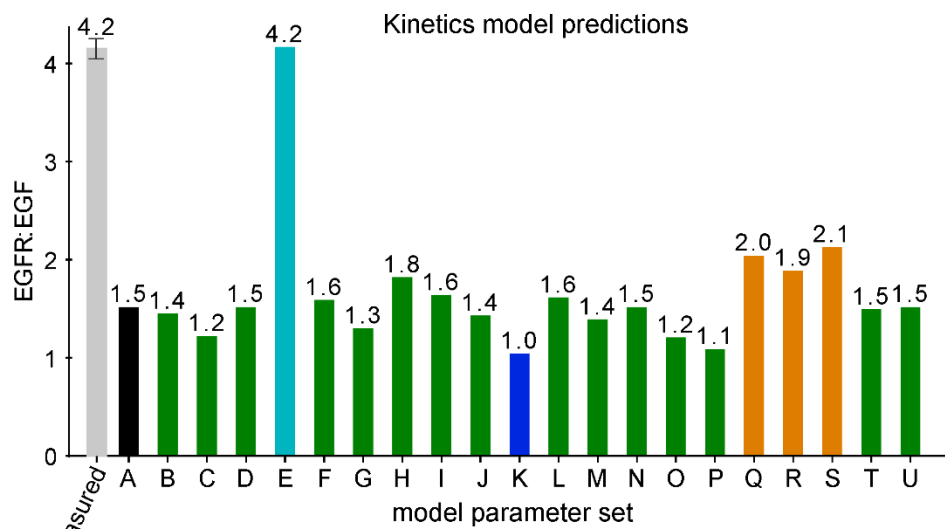


Figure S9: Characterization of EGFR and EGF foci stoichiometry after addition of EGF. (a) Percentage of EGFR tracks colocalized to EGF. (b) Number of colocalized EGF-EGFR tracks detected per cell (with s.d. error bars) versus time (c) EGFR-GFP foci stoichiometry (number of molecules per foci) versus time (with s.d. error bars) for EGF-colocalized and not colocalized after EGF addition, and before EGF addition.

Figure S10. Time-dependent EGFR-EGF kinetics model explains observations if EGF cannot bind receptor dimers. (a) Schematic of reactions considered by the model: ligand binding to receptor monomers/dimers, receptor dimerization, endocytosis, and recycling. (b) Results of kinetics model for time dependence of receptor concentrations (for ligated and unligated monomers and dimers, and internalized components) choosing baseline parameters corresponding to 37°C (see Figure S11). **Inset:** fractional saturation Y_{surface} equal to EGF:EGFR ratio (we experimentally measure its inverse, EGFR:EGF ratio). (c) Model predictions for same parameters as in (a) but assuming ligand binds only to monomers. (d) Model predictions for EGFR:EGF ratio (inverse of Y_{surface}) for several conditions (see Figure S10). Higher ratios in agreement with our data (grey bar) are obtained when ligand cannot bind to dimers (light blue). (e) Equilibrium Y_{surface} versus EGF concentration for parameters shown in (a) and (b), as well as for reaction rates at 4°C. Black dashed line: experimental EGF concentration. Red dashed arrow: equivalent mean value of EGFR:EGF that we measure experimentally.





Model parameter sets

| | |
|---|---|
| A | baseline parameters |
| B | mild positive cooperativity ($k_{22,on} = k_{11,on}$, $k_{22,off} = k_{11,off}$) |
| C | strong positive cooperativity ($k_{22,on} = 10k_{11,on}$, $k_{22,off} = k_{11,off}$) |
| D | extreme negative cooperativity ($k_{22,on} = 0$) |
| E | ligand cannot bind to RR dimers ($k_{21,on} = 0$) |
| F | ligand cannot bind to monomers ($k_{11,on} = 0$) |
| G | all ligand binding on-rate constants increase x2 |
| H | all ligand binding on-rate constants decrease %2 |
| I | all ligand binding off-rate constants increase x2 |
| J | all ligand binding off-rate constants decrease %2 |
| K | 4°C rates |
| L | increased endocytosis rate ($k_{endoc}=10\%/min$) |
| M | reduced endocytosis rate ($k_{endoc}=3\%/min$) |
| N | increased recycling rate ($k_{recycle}=40\%/min$) |
| O | zero recycling rate ($k_{recycle}=0\%/min$) |
| P | no R-RL (hetero) dimerization ($l_{21,on}=0$) |
| Q | no R-R (homo) dimerization ($l_{20,on}=0$) |
| R | no RL-RL (homo) dimerization ($l_{22,on}=0$) |
| S | no R-R or RL-RL (homo) dimerization ($l_{20,on}=0$, $l_{22,on}=0$) |
| T | reduced total no. of receptors ($R_{total}=200,000$) |
| U | increased total no. of receptors ($R_{total}=400,000$) |

Figure S11. Kinetics model predictions for various parameter sets. Predictions of EGFR:EGF ratio (inverse of $\gamma^{surface}$) for baseline parameters (black bar, see details below) as well as for parameter sets (B to U) corresponding to a change with respect to the baseline parameters as indicated in the table below the graph. The plot shows that increased EGFR:EGF ratios closer to the experimentally measured value ~ 4 (grey bar) are predicted by the model for strongly reduced (absent) ligand binding to RR dimers (light blue bar). Reducing R-R and RL-RL homo-dimerization also leads to somewhat increased EGFR:EGF ratios ~ 2 (orange bars). Use of 4°C reaction rates leads to EGFR:EGF ~ 1 (dark blue bar). Baseline parameters are: $R_{total}=310,000$ molecules, $[L]=15.6$ nM; $k_{11,on} = 10^6 M^{-1}s^{-1}$, $k_{11,off} = 10^{-3} s^{-1}$, $k_{21,on} = k_{11,on}$, $k_{21,off} = k_{11,off}$, $k_{22,on} = k_{11,on}/7$ and $k_{22,off} = 2 \times k_{11,off}$ so that $K_{11} = 10^9 M^{-1}$, $K_{21} = K_{11}$, $K_{22} \approx K_{11}/14$; $l_{20,on} = 10^{-4} (molecules/cell)^{-1}s^{-1}$, $l_{20,off} = 10^{-1} s^{-1}$, $l_{21,on} = l_{20,on}$, $l_{21,off} = l_{20,off}$, $l_{22,on} = l_{20,on}/5$ and $l_{22,off} = 2 \times l_{20,off}$, so that $L_{20} = 10^{-3} (molecules/cell)^{-1}$, $L_{21} \approx L_{20}$ and $L_{22} \approx L_{20}/10$; $k_{endoc} = 6\%/min$, $k_{recycle} = 10\%/min$.

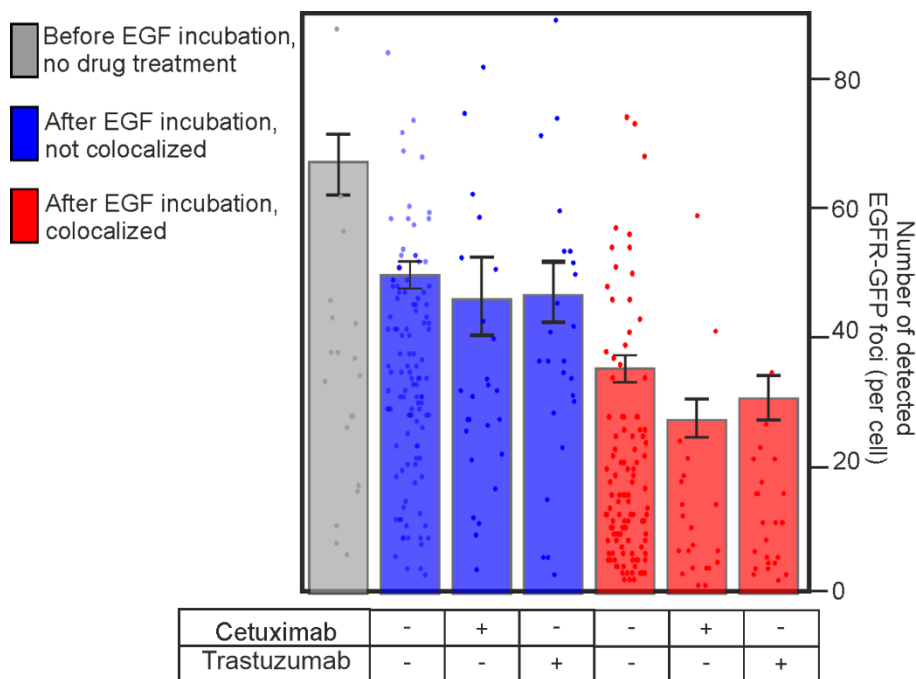


Figure S12: Number of EGFR-GFP foci detected per cell. EGF-colocalized EGFR foci (red) and non-colocalized EGFR foci (blue) are shown. The table below indicates + or - for addition or not of anti-cancer drugs cetuximab and trastuzumab. Data before EGF incubation in the absence of drugs is shown as a grey bar. Error bars are s.d, N=10-117 cells per dataset.

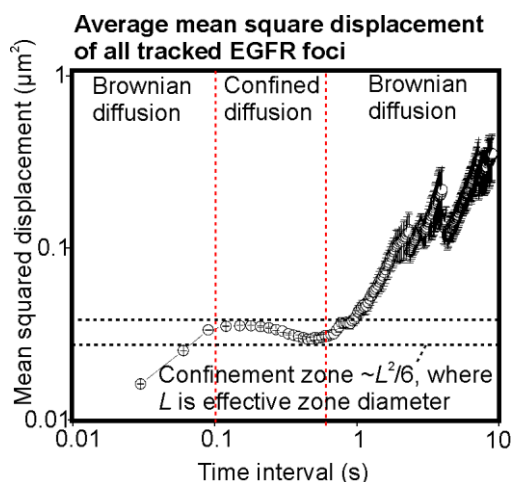


Figure S13: EGFR foci average mean square displacement vs time. Log-log plot for average mean square displacement vs. time interval for all collated EGFR-GFP foci tracks before addition of EGF, putative confinement zone indicated (dashed lines), from number of foci N=770, acquired from number of cells N=19.

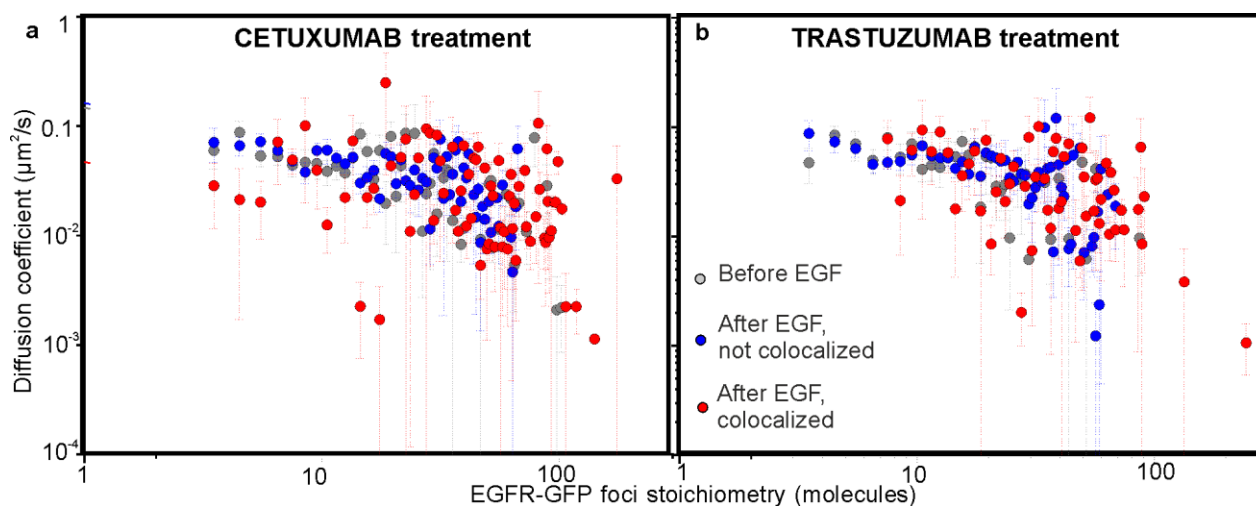


Figure S14: EGFR foci diffusion and anti-cancer drug treatment effects. Log-log plots for variation of apparent diffusion coefficient D with EGFR stoichiometry S , for cells treated with drugs cetuximab (a) and trastuzumab (b).

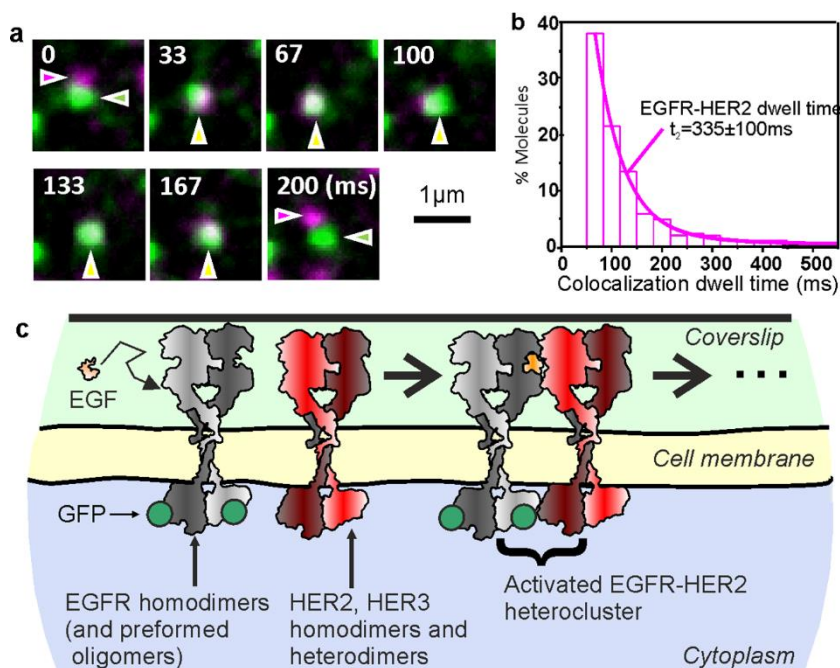


Figure S15. HER2-EGFR interactions. (a) Single-molecule TIRF images of EGFR-HaloTag650 (magenta arrows) and HER2-GFP (green arrows) undergoing transient colocalization and co-diffusion (yellow arrows) in CHO-K1 cells. Time since start (ms) is indicated. (b) Histogram for the dwell time of colocalized EGFR/HER2 foci. A double exponential fit to these data is overlaid, showing the EGFR-HER2 dwell time $t_d = 335 \pm 100$ ms. (c) Schematic diagram of the cell membrane and cytoplasm showing the interaction between EGFR homodimers (and preformed oligomers) and HER2, HER3 homodimers and heterodimers, leading to an activated EGFR-HER2 heterocluster.

and the mean and error (95% confidence bound) indicated for the average colocalization dwell time between *HER2* and *EGFR*. Data extracted from $N=4$ cells corresponding to 400 colocalization detected events with random apparent colocalization dwell times assessed using 285 detected events. (c) Schematic illustrating how *HER2/HER3* and *EGFR* dimers might associate following *EGF* ligation, although we do not exclude monomer receptors also interacting.

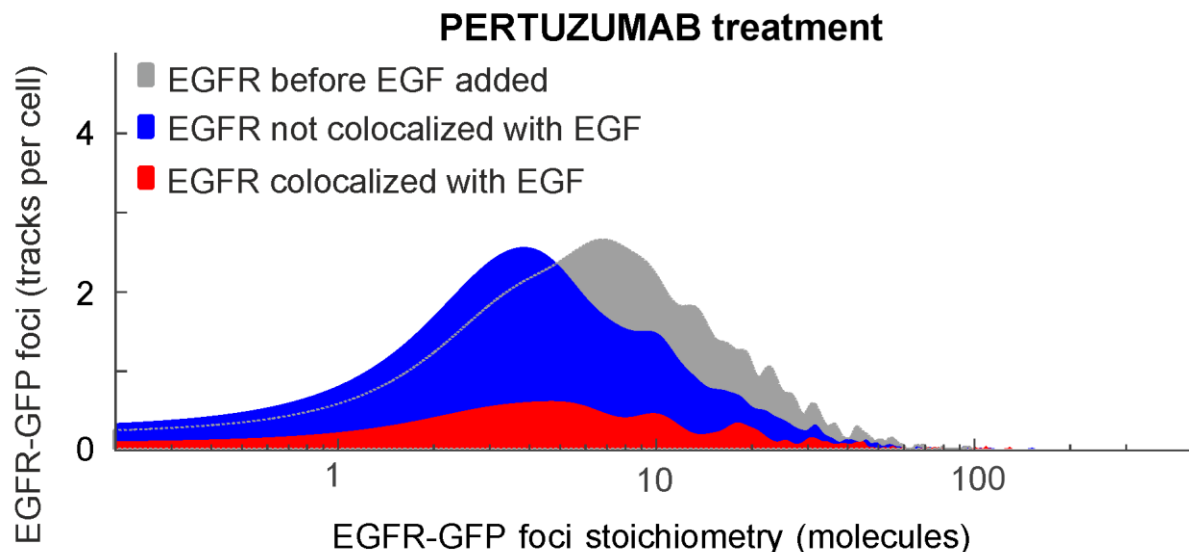


Figure S16. Effect of pertuzumab on *EGFR* foci stoichiometry. Distribution of *EGFR* foci stoichiometry for cells treated with pertuzumab or, showing pre (grey) and post *EGF* addition for *EGF-EGFR* (red) and unligated *EGFR* (blue) foci, data collated across 60 min *EGF* incubation time. Number of cells per dataset in the range $N=21$.

Supplementary Tables

| Biochemical intervention | | | | EGFR foci stoichiometry, not colocalized with EGF | | EGFR foci stoichiometry, colocalized with EGF | | N cells | N tracks/cell |
|--------------------------|---|---|--|---|----------|---|----------|---------|---------------|
| E | C | T | | Mean \pm s.e.m (molecules per EGFR cluster) | N tracks | Mean \pm s.e.m (molecules per EGFR cluster) | N tracks | | |
| - | - | - | | 12.8 \pm 0.4 | 1,250 | N/A | N/A | 19 | 66 |
| + | - | - | | 10.8 \pm 0.2 | 4,741 | 31.1 \pm 1.1 | 1,969 | 117 | 57 |
| - | + | - | | 19.9 \pm 1.0 | 531 | N/A | N/A | 10 | 53 |
| - | - | + | | 15.3 \pm 0.7 | 408 | N/A | N/A | 10 | 41 |
| + | + | - | | 18.8 \pm 0.5 | 916 | 51.0 \pm 2.1 | 303 | 25 | 37 |
| + | - | + | | 16.8 \pm 0.4 | 1,273 | 44.2 \pm 2.4 | 334 | 27 | 47 |

Table S1. Mean EGFR cluster stoichiometry. Total number of tracks (*N tracks*) and number of individual cells (*N cells*) in the datasets are indicated. Biochemical interventions are: incubation with EGF (*E*), treatment with drug cetuximab (*C*) or treatment with drug trastuzumab (*T*), shown on the left-hand-side columns (- for no intervention, + for intervention).

Supplementary movie legends

Movie S1. Single-colour TIRF imaging of live transfected SW620 cells. TIRF movie showing two adjacent cells transfected with EGFR-GFP (green) before addition of EGF.

Movie S2. Dual-colour TIRF imaging of live transfected

SW620 cells. TIRF movie showing a single cell transfected with EGFR-GFP (green), 10 minutes post addition of EGF-TMR (red, 100 ng/ml).

Movie S3. Dual-colour TIRF imaging of live CHO-K1 cell. TIRF movie showing a single CHO-K1 cell transfected with GFP-labelled HER2 (green) and HaloTag650-labelled EGFR (magenta).

Movie S4. Zoom into dual-colour TIRF imaging of live CHO-K1 cells. Zoom-in of cell shown in movie S3 displaying transient co-diffusion of HER2 and EGFR molecules.

Supplementary references

75. S. Sigismund, *et al.*, Clathrin-independent endocytosis of ubiquitinated cargos. *Proc. Natl. Acad. Sci. U. S. A.* **102**, 2760–2765 (2005).
76. P. J. Enriori, *et al.*, Breast cyst fluids increase the proliferation of breast cell lines in correlation with their hormone and growth factor concentration. *Clin. Endocrinol. (Oxf)*. **64**, 20–28 (2006).
77. X. Michalet, Mean square displacement analysis of single-particle trajectories with localization error: Brownian motion in an isotropic medium. *Phys. Rev. E* **82**, 041914 (2010).
78. K. G. N. Suzuki, *et al.*, Transient GPI-anchored protein homodimers are units for raft organization and function. *Nat. Chem. Biol.* **8**, 774–83 (2012).
79. A. Kusumi, *et al.*, Paradigm shift of the plasma membrane concept from the two-dimensional continuum fluid to the partitioned fluid: High-speed single-molecule tracking of membrane molecules. *Annu. Rev. Biophys. Biomol. Struct.* **34**, 351–378 (2005).
80. J. Barretina, *et al.*, The Cancer Cell Line Encyclopedia enables predictive modelling of anticancer drug sensitivity. *Nature* **483**, 603–607 (2012).
81. M. R. Holbrook, J. B. O'Donnell, L. L. Slakey, D. J. Gross, Epidermal growth factor receptor internalization rate is regulated by negative charges near the SH2 binding site Tyr992. *Biochemistry* **38**, 9348–56 (1999).
82. S. Felder, J. LaVin, A. Ullrich, J. Schlessinger, Kinetics of Binding, Endocytosis, and Recycling of EGF Receptor Mutants. *J. Cell Biol.* **117**, 203–212 (1992).
83. R. S. Kasai, *et al.*, Full characterization of GPCR monomer-dimer dynamic equilibrium by single molecule imaging. *J. Cell Biol.* **192**, 463–480 (2011).